Variability of Radiative Cooling during the Asian Summer Monsoon and Its Influence on Intraseasonal Waves

AMITA V. MEHTA

Universities Space Research Association, NASA/Goddard Space Flight Center, Greenbelt, Maryland

ERIC A. SMITH

Department of Meteorology and Supercomputer Computations Research Institute, The Florida State University, Tallahassee, Florida

(Manuscript received 9 November 1995, in final form 10 July 1996)

ABSTRACT

Infrared radiative cooling rates are calculated over the Asian summer monsoon between 5°S–20°N and 40°–135°E at a spatial resolution of 5° × 5° for the summer seasons of 1984 and 1987. A medium spectral resolution infrared radiative transfer model with specified temperature, moisture, clouds, and trace gas distributions is used to obtain the cooling rate profiles. Cloud distributions for the two summers are obtained from Indian National Satellite measurements. Seasonal mean and intraseasonal variations of clouds and radiative cooling rates over a 21–76-day range of periods are examined.

The analysis identifies centers over the central and eastern Indian Ocean, and western Pacific Ocean, along the equator, and along 15°N, where seasonal mean cloud amounts range from 40% to 80% with cloud tops mostly in the middle and upper troposphere. Intraseasonal variability of clouds is also large over these centers (% variances >25%). Consistently, seasonal mean cooling rates are at a maximum (3°–5°C day^{-1}) in the upper troposphere between 300 and 400 mb, related to cloud-top cooling. The cooling rates below 400 mb are between 1° and 3°C day^{-1}. The cooling rates exhibit intraseasonal amplitudes of 1.0°–1.5°C day^{-1}. The largest amplitudes are found between 300 and 500 mb, indicating that cooling rate variability is directly related to intraseasonal variability of convective clouds. Spatial distributions of clouds and cooling rates remain similar during the 1984 and 1987 summer seasons. However, during 1987, intraseasonal amplitudes of deep convective cloud amount and cooling rate over the Indian Ocean are 10%–15% larger than in 1984.

It is shown that intraseasonal variability of cooling rates over the Indian Ocean can perturb convective heating by 10%–30% in the upper and lower troposphere. Based on a one-dimensional radiative–convective equilibrium model, it is estimated that the radiative damping timescale over the Indian Ocean region is ~3 days. Based on this damping timescale and in conjunction with a model of equatorial Kelvin waves with first baroclinic mode, it is hypothesized that the variable cloud-radiative cooling rates can alter phase speeds of Kelvin waves by up to 60%. This helps explain why the frequency range of intraseasonal oscillations is so broad.

1. Introduction

During the past two decades, following the study by Madden and Julian (1971), there have been numerous studies about intraseasonal variability in the tropical atmosphere on a timescale of 20–60 days; see review of Madden and Julian (1994). The zonal wind, streamfunction, and velocity potential exhibit intraseasonal disturbances that propagate eastward around the globe in the tropical belt throughout the year and northward in the Indian monsoon region during the summer season (Mehta and Ahlquist 1986; Knutson and Weickmann 1987; Mehta and Krishnamurti 1988). On the other hand, intraseasonal variability of deep convective clouds, as derived from outgoing longwave radiation (OLR), is found to be confined over the tropical Indian and western Pacific Oceans (Lau and Chan 1986; Murakami et al. 1986; Knutson and Weickmann 1987; Zhu and Wang 1993). Also, over the Arabian Sea, the Bay of Bengal, the equatorial Indian Ocean, the South China Sea, and the western Pacific Ocean, localized centers are found where deep convection shows strong intraseasonal variability (Smith and Mehta 1990). Also, cloud and convection variability over the Indian Ocean are closely related to Indian monsoon activity (Sikka and Gadgil 1980; Yasunari 1980; Smith 1984; Smith and Sikka 1987).

Due to the structure and eastward propagation of zonal wind disturbances and their association with convective activity in the Indian and western Pacific Oceans,

Corresponding author address: Eric A. Smith, Dept. of Meteorology and Supercomputer Computations Research Institute, The Florida State University, Tallahassee, FL 32306.
E-mail: esmith@metsat.met.fsu.edu

the widely accepted explanation is that intraseasonal disturbances are equatorial Kelvin waves forced by convective heating; see Rui and Wang (1990) and Hendon and Salby (1994), plus references therein. Simple models of intraseasonal variability emphasize this idea and show that convective heating resulting from large-scale moisture convergence plays a major role in exciting and maintaining equatorial waves with intraseasonal timescales (Hayashi and Sumi 1986; Lau and Peng 1987; Chang and Lim 1988; Hendon 1988; among others). Atmospheric general circulation models (GCMs) have also been able to simulate eastward propagating intraseasonal waves (Goswami and Shukla 1984), some supporting the notion that they are Kelvin waves; see Slingo and Madden (1991) and references therein.

Although observational and modeling studies have clarified the structure of intraseasonal waves, their origin and their variability are not fully understood. One of the more intriguing questions is why there is such a broad range of periodicities in the behavior of the waves. Observational studies have reported periodicities extending from 6 to 70 days (e.g., Kiladis and Weickmann 1992). Based on OLR and atmospheric circulation data analysis, Kiladis and Weickmann (1992) pointed out multiscale intraseasonal oscillations with periodicities of 6–14, 14–30, and 30–70 days. They propose that atmospheric circulation patterns associated with these different timescales are different, and suggest that 30–70-day variability is related to tropical heating, whereas the shorter period variability is likely due to teleconnections with the extratropics. Lau et al. (1994) also support this notion. Interannual variations of the periodicity and amplitude and the sporadic nature of intraseasonal wave propagation have also been noted by Mehta and Krishnamurti (1988).

Modeling experiments have had difficulty in simulating the observed range of phase speeds of intraseasonal waves. In most models, intraseasonal waves generally tend to propagate faster than those observed in the atmosphere. Various modeling studies indicate that the phase speeds of intraseasonal waves are very sensitive to the vertical distribution of diabatic heating and tropospheric stability (Lau et al. 1988; Swinbank et al. 1988). For example, Lau and Peng (1987) and Sui and Lau (1989) found that maximum heating in the lower troposphere favors wave propagation closer in line with observed phase speeds. However, the manner in which the diabatic heating profile is obtained in most model experiments, that is, dominated by the convective heating term, leads to the heating peaking in the middle troposphere. It is likely that this heating configuration in the models is what excites intraseasonal waves with phase speeds faster than those observed.

In the tropical atmosphere, net diabatic heating results from a delicate balance between two large diabatic components, namely, latent heating and longwave radiative cooling (Slingo and Slingo 1988). This is particularly so in the presence of clouds since radiative profiles are strongly modulated due to differential radiative cooling at cloud top and cloud base. Over the Indian and western Pacific Oceans, where intraseasonal waves are believed to be strongly forced, cloudiness exhibits clear intraseasonal variability accompanied by strong cloud-radiative forcing (see Ramanathan 1987; Smith and Smith 1987).

If phase speeds of intraseasonal waves are as sensitive to the heating profile as indicated by the studies cited above, there is a possibility that convective heating may not be the sole control on phase speeds. If radiative cooling can modify the convective heating profile, it may also partially control the phase speed of intraseasonal waves. Evidence of this can be found in Slingo and Madden's (1991) study. They examined the impact of longwave cloud-radiative effects on the phase speed of intraseasonal waves using a GCM. When cloud-radiative effects were excluded, the phase speed of the intraseasonal waves increased, corresponding to a decrease in period of 7–8 days. Although they did not consider this change in phase speed to be statistically significant, their results suggested that infrared radiative cooling provides a mechanism that alters wave propagation speed.

Detailed observational estimates of radiative cooling rate profiles over the Indian and western Pacific Oceans, where intraseasonal waves are believed to originate, are scarce; see Smith and Shi (1995). Some of the earlier estimates of monthly mean radiative cooling distributions over the Northern Hemisphere were provided by Katayama (1967). Dopplick (1972) later calculated longitudinally averaged, seasonal mean radiative cooling profiles as a function of latitude. But in both of those early studies, clouds were included in a highly simplified climatological fashion. At tropical latitudes, Cox and Griffith (1979a,b) estimated radiative cooling rates over the Global Atmospheric Research Program (GARP) Atlantic Tropical Experiment (GATE) region, and more recently Ackerman and Cox (1987) estimated the same over the Indian monsoon region for a few selected days during the First GARP Global Experiment period. These latter two studies explicitly included the effects of cloudiness. However, it is fair to say that there is very little observational literature concerning the intraseasonal modulation of infrared cooling by cloudiness and its influence on tropical circulations.

The objective of this study is to calculate observationally based, cloud-modulated radiative cooling rates over the Indian and western Pacific Ocean regions, and then analyze cooling rate profiles focusing on their intraseasonal variability. The analysis will show that intraseasonal variability of the cooling rate profiles can perturb convective heating profiles by up to 30% in the lower and upper troposphere. From these calculations, a one-dimensional radiative–convective equilibrium model is used to estimate the radiative damping timescale over the Indian and western Pacific Oceans. We speculate, based on a two-level model of equatorial Kel-

vin waves, that the phase speeds of such waves excited by convective heating can be altered due to the radiative damping effect. The result is a range of timescales of propagation providing a possible explanation for the broad range of periodicities that has been associated with such waves. We note these calculations only provide a means to gauge the magnitude of the feedback effect of cloud-radiative cooling, not a mechanism that actually generates the intraseasonal waves.

Infrared cooling rates are calculated from a medium spectral resolution infrared radiative transfer model. The effects of cloudiness on cooling rates are treated explicitly using geostationary satellite measurements from the Indian National Satellite (INSAT). The cooling rates are obtained on a $5^\circ \times 5^\circ$ latitude–longitude grid over a domain between 5°S–20°N and 40°–135°E. This is the domain over which cloudiness and OLR observations have shown maximum intraseasonal variability. Since Indian monsoon activity is found to be closely linked to global-scale intraseasonal waves (Mehta and Krishnamurti 1988), two very different summer monsoon seasons are chosen for the analysis, that is, 1984 and 1987. During 1984, normal to above-normal rainfall occurred, whereas during 1987, below-normal rainfall occurred over the Indian monsoon region; see articles in the *Mausam* journal by Staff Members (1985, 1988). A 152-day interval between 17 May and 15 October was selected for the analysis. This period extends over various phases of the summer monsoon. Similarities and differences of cloudiness and cooling rates during the two seasons are noted. The radiative transfer model and input data needed to calculate the cooling rates are described in section 2. Section 3 discusses the sensitivity of the cooling rate retrievals to the specified inputs. Section 4 presents the results of the analysis, while section 5 examines the possible feedback of cloud-induced radiative cooling on the phase speeds of intraseasonal waves. Section 6 provides the summary and conclusions of the study.

2. Calculation of radiative cooling rates

a. Radiative Transport Model (RTE)

A radiative transfer model covering the spectral range between 2 and 250 μm (5000–40 cm^{-1}) is used to calculate vertical profiles of directional fluxes and cooling rates for clear and cloudy atmospheric layers. The model considers both line and continuum absorption due to water vapor, along with absorption due to ozone and carbon dioxide (combined with the other uniformly mixed gases of N_2O, CH_4, CO, N_2, and O_2), and finally absorption due to cloud. It uses random band models based on transmittance formulations to account for gaseous absorption (Goody 1952; Malkmus 1967). The parameterization of flux transmittance for the H_2O continuum is based on Clough et al. (1981). Clouds are considered gray with emissivities parameterized in terms of cloud liquid and ice water paths following Stephens (1978a,b) and Paltridge and Platt (1981). To provide microphysical sensitivity, liquid and ice absorption coefficients are adjusted for the assumed effective hydrometeor radius (r_{eff}) following Smith and Shi (1992) and Stephens et al. (1990). Values of r_{eff} are set to 10 and 20 μm for water and ice clouds, respectively; see Prupracher and Klett (1980). A more detailed description of the model design and its calibration is found in Mehta (1991). The model was validated by comparing its directional fluxes with a set of line and band model calculations provided by the Intercomparison of Radiation Codes for Climate Models (ICRCCM); see Luther et al. (1988) and Ellingson et al. (1991). Model fluxes are within 1% agreement to the ICRCCM mean fluxes for cloud-free cases, and within 2.5% for cloudy cases.

Longwave radiative cooling rate profiles are obtained at $5^\circ \times 5^\circ$ spatial resolution over the study area. The following sections describe how the profiles of atmospheric temperature, water vapor mixing ratio, and ozone; the background carbon dioxide concentration; the surface skin temperatures and emissivities; and the cloud variables of cloud amount, cloud-top height, cloud-base height, and vertical cloud liquid/ice water content structures have been specified.

b. Atmospheric temperature and gaseous constituent profiles

Atmospheric temperature and water vapor mixing ratio profiles for the two summer seasons of 1984 and 1987 were obtained from the European Centre for Medium-Range Weather Forecasts objectively analyzed global datasets (hereafter referred to as ECMWF profiles). Daily profiles for the study area have been extracted using 7 pressure levels (1000, 850, 700, 500, 300, 200, and 100 mb) for the $5^\circ \times 5^\circ$ grids. Above 100 mb, tropical climatological profiles of temperature and water vapor mixing ratio from McClatchey et al. (1972) are used such that the extended profiles are continuous and differentiable at the attachment level. For ozone, a tropical climatological profile is also obtained from McClatchey et al. (1972). Carbon dioxide concentration is set uniformly to 340 parts per million by volume, consistent with the mean global concentration for the 1984–87 period.

c. Skin temperature and cloud retrieval from INSAT measurements

1) DESCRIPTION OF INSAT GEOSTATIONARY SATELLITE

INSAT geostationary satellites are nominally located near 75°E, providing coverage of the Indian Ocean. They carry spinscan cameras measuring radiances in the 0.5–0.7 μm visible and 10.5–12.5 μm infrared (IR) window regions. Measurements from the IR channel are calibrated to equivalent blackbody temperature (EBBT).

For these calculations, a special dataset made available through the National Center for Atmospheric Research and described by Smith et al. (1989), has been used. The dataset consists of twice-per-day infrared images at 0000 and 1200 UTC, at a spatial resolution of 22 km; see Lamm et al. (1991).

INSAT provides uninterrupted observations of cloud systems over the Indian Ocean sector. For the cooling rate calculations, daily INSAT images from 17 May to 15 October during 1984 and 1987 have been used to construct EBBT time series over the $5^\circ \times 5^\circ$ grid mesh. At 22 km resolution, each subgrid contains from 400 to 625 EBBT pixels, depending on its location with respect to the satellite subpoint. To form the two time series, we have selected one image per day at 1200 UTC.

2) SKIN TEMPERATURE RETRIEVAL

Skin temperatures are obtained from the INSAT EBBTs after filtering out cloudy pixels and correcting for attenuation due to water vapor absorption. For oceanic and continental backgrounds, surface emissivites are taken as 0.95 and 0.98 (Sellers 1965). The compositing technique used by Rossow et al. (1985) for generation of the International Cloud Climatology Project (ISCCP) cloud datasets is applied to first obtain time series of cloud-free EBBTs from the two 17 May–15 October time periods. Accordingly, for each daily EBBT image, a 31-day sliding window centered on that day is first defined. At each pixel location in the EBBT image, the maximum EBBT value occurring during the 31-image sequence is considered to be the most likely cloud-free EBBT for that pixel with respect to the day on which the 31-day window is centered. It is presumed that after this operation is completed, there remain residual cloudiness effects due to persistent cloud fields. To reduce such effects, a low-pass filter is applied to remove high-frequency variations from the time series at each pixel location. The filtered cloud-free EBBTs are then corrected for water vapor attenuation using a regression procedure suggested by Cogan and Willand (1976) based on precipitable water (PW) as the independent variable. The PW values are obtained from the ECMWF profiles. The corrected cloud-free EBBTs are finally averaged over the subgrids to obtain the estimates of skin temperature. To avoid unrealistic differences between skin temperature and surface air temperature, as designated by ECMWF profiles, the differences at each subgrid location are restricted to one standard deviation from the seasonal mean difference, accomplished by adjusting the retrieved skin temperatures to obey this constraint.

During both years, seasonal mean oceanic skin temperatures retrievals are between 295 and 301 K and compare well with the climatological data of Bottomley et al. (1990). Over the continental regions, skin temperatures run higher than 300 K, with warmest temperatures of $\sim$320 K found over the Arabian Peninsula.

3) CLOUD AMOUNT AND CLOUD-TOP HEIGHT RETRIEVAL

Cloud amount (percentage of area covered by clouds) and cloud-top height distributions necessary for the cooling rate calculations are also retrieved from the EBBT measurements. Over each subgrid, cloud amount is first obtained by identifying the cloudy pixels using an infrared threshold method similar to that described by Rossow et al. (1985). Accordingly, each pixel is considered to be cloudy if the associated EBBT value is colder than the cloud-free EBBT by a threshold temperature of 6°C. This threshold is consistent with that used in ISCCP calculations (see Rossow 1989).

Cloudy pixels over each subgrid are further classified into several cloud clusters with varying cloud-top temperatures. A dynamical clustering method similar to that described in Debois et al. (1982) is used to classify the cloud clusters. The underlying concept is to identify clusters with high population densities in the EBBT histograms. The clusters statistically represent dominant cloud-top height categories, with the percentage of pixels in each cluster representing cloud amount for that category. In addition, the mean EBBT of all pixels in a cluster is considered to represent the representative cloud-top temperature for that category. A maximum of six such clusters are allowed at each subgrid position. Cloud-top pressure and height for each cloud cluster are obtained by matching the representative cloud-top temperatures to the appropriate temperature levels in the associated ECMWF profile.

The final cloud clusters are classified as low, middle, and high cloud according to assigned cloud-top heights. The following subsection explains that this classification also affects the assignment of cloud-base heights for each cloud cluster. A threshold of 2 km is used to separate low and middle clouds, while one of 7 km separates middle and high clouds. These thresholds have been used by Stowe et al. (1988) in classifying low, middle, and high clouds from *Nimbus-7* measurements.

Although the INSAT-derived clouds can be classified according to their estimated cloud-top heights, it is not possible to separate cirrus clouds from other middle and high cloud categories using only single-channel infrared EBBTs. This distinction is important in RTE calculations because the radiative properties of cirrus are different than, for example, those of deep cumulus congestus. To make the distinction, a cirrus cloud climatology derived from six years of *Nimbus-7* measurements (1979–84) is used to separate cirrus from the INSAT-derived middle and high clouds. In the *Nimbus-7* cloud detection scheme, cirrus clouds are identified as a fraction of middle and high clouds (Stowe et al. 1988). We have derived statistical regression coefficients between the *Nimbus-7* cirrus cloud amounts and the INSAT middle and high cloud amounts for each month and latitude. These are then used to estimate daily cirrus amounts as a fraction of the middle and high cloud

TABLE 1. Cloud parameters for subgrid centered at 15°N, 120°E on 15 June 1984.

Cloud cluster number	Cloud amount (%)	Cloud-top EBBT (K)	Cloud-top pressure (mb)	Cloud-top height (km)
1	12.2	262.8	452	6.9
2	15.8	246.4	327	9.3
3	15.5	233.4	261	10.9
4	12.7	224.5	220	12.08
5	28.3	215.9	171	13.7
6	14.4	206.3	122	15.1

Cloud cluster number	Cloud amount distribution between thick and thin clouds (%)		Cloud-base pressure (mb)		Cloud water content ($g\ m^{-3}$)
	Thick	Thin	Thick	Thin	
1	6.4	6.4	970	552	0.150
2	13.5	2.3	970	427	0.650
3	13.2	2.3	970	361	0.390
4	10.4	2.3	970	320	0.027
5	26.0	2.3	970	271	0.018
6	12.1	2.3	970	222	0.130

amounts from INSAT. The INSAT-derived cloud amounts and their vertical distributions during the two years are discussed in section 4a.

d. Cloud-base height assignment

Cloud-base heights are also required for the cooling rate calculations. It is not possible to obtain cloud bases directly from satellite infrared measurements. Moreover, there is no source of observations on cloud bases within the monsoon region. Therefore, we have adapted the approach taken by Cox and Griffith (1979a) and Ackerman and Cox (1987) to assign cloud bases. Here, clouds are assumed to be either thick or thin depending on their cloud-top height. All thick clouds have their bases assigned to the lifting condensation level (LCL), whereas thin clouds have their bases assigned 100 mb below their cloud-top pressure levels.

The division of cloud amounts between thick and thin is based on the cloud-top heights. As discussed previously, cloud amounts and cloud-top heights are found from the cloud clustering algorithm. At each subgrid position, cloud clusters with their tops at or below 2 km are assigned their bases at the diagnosed LCL. For cloud clusters with tops between 2 and 7 km, cloud amounts are equally distributed among the cloud bases at the LCL and at 100 mb below the cloud-top pressure level. This partitioning assumes that some clouds are convective and some are of the thin, stratiform variety. Cloud clusters with tops above 7 km are considered to be cirrus or deep convective clouds. The cirrus amount is obtained first, based on the previously described regression procedure used in conjunction with the INSAT-derived middle and high cloud amounts. This cloud amount is equally distributed among all cloud clusters with tops above 7 km, with bases assigned 100 mb below cloud tops. The remaining cloud amount is assumed to consist of deep convective clouds, which are assigned bases at the LCLs. The assumptions concerning convective and stratiform cloud types for the summer monsoon region are consistent with the cloudiness analysis of Johnson and Houze (1987). The approach to partitioning cirrus is supported by the Warren et al. (1985) study, which indicates tropical cirrus occurs mostly in areas of deep convection. Table 1 provides an example of how cloud amount for various cloud clusters within a subgrid centered at 15°N, 120°E (15 June 1984) is distributed among thick and thin cloud bases.

TABLE 2. Cloud water content as function of cloud-top pressure (from Cox and Griffith 1979a).

Pressure (mb)	Cloud water content ($g\ m^{-3}$)
100	0.01
200	0.02
300	0.05
400	0.10
500	0.20
600	0.33
700	0.50
800	1.0
900	1.0
1000	1.0

e. Cloud water content assignment

In the RTE calculations, as indicated in section 2a, cloud emissivities are parameterized in terms of liquid and ice water paths within the cloud. Observations of the latter quantities are not available over the monsoon domain. As discussed by Ackerman and Cox (1987), observational studies have shown a wide range of cloud water contents for a variety of environments. In order to provide a systematic representation of this parameter, cloud water content is considered to be a function of cloud-top pressure, based on measurements that were taken during GATE; see Cox and Griffith (1979a). This same distribution was used in the study by Ackerman and Cox (1987), which investigated the radiation budget of the Indian monsoon. The relevant cloud water content vertical distribution is given in Table 2. For each cloud cluster identified within the monsoon subgrids, cloud water content is assigned according to its cloud-top pressure using the distribution given in Table 2. Cloud water content is considered to be homogeneous within the cloud column. For purposes of assigning cloud-radiative properties, any cloud water occurring above the freezing level is assumed to be in the form of ice.

The above parameters are used as inputs to the radiative transfer model. The vertical resolution of the model is 100 mb, but cloud-top and cloud-base levels can be specified arbitrarily at model levels falling between the standard levels. RTE calculations are first

made assuming cloud-free columns and then for each cloud structure category based on the cluster analysis. Total directional fluxes at any atmospheric level for a given subgrid are obtained by taking linear combinations of the contributions from the clear and cloudy fluxes. Time series of cooling rates are then obtained from the directional fluxes for the summer seasons of 1984 and 1987.

3. Sensitivity of radiative cooling rates to parameter input

It is difficult to judge absolute accuracy of the calculated cooling rates, since direct observations of radiative fluxes and cooling rates over the Asian monsoon region are scarce. By the same token, as mentioned in section 2a, the radiative transfer model used in the calculations performed very well in a calibration against the pool of radiative transfer models used in the ICRCCM intercomparisons.

To assess the credibility of the overall modeling scheme in conjunction with the assumptions used in specifying model input parameters, a number of sensitivity tests have been carried out. First, model performance is assessed by comparing calculated outgoing fluxes in the 10.5–12.5 μm band against outgoing fluxes derived directly from INSAT EBBTs. A total of 3600 subgrids covering the entire monsoon domain over the period 17 May–15 June were analyzed. The mean flux difference and standard deviation during 1984 are 8.6 W m^{-2} and 2.2 W m^{-2}, while during 1987 they are 9.3 W m^{-2} and 2.4 W m^{-2}. During both seasons there is a slight, nearly linear bias such that flux differences are larger at low cloud amounts, decreasing as cloud amount increases. The bias stems mostly from two sources. At lower cloud amounts, flux differences are primarily due to the inaccuracies in specification of skin temperatures and the atmospheric temperature and moisture profiles. As cloud amounts increase, flux differences are affected by overestimation of cloud amounts introduced by the infrared threshold method, which classifies each INSAT footprint as either completely cloudy or completely clear. However, the overall differences between modeled fluxes and INSAT-derived fluxes are small and consistent throughout both seasons. As suggested by the Ellingson et al. (1991) analysis of ICRCCM results, these differences are synonymous with uncertainties in state-of-the-art models, so in that sense, the flux differences found here are minor.

The cooling rates are also compared with earlier estimates provided by Katayama (1967). Figure 1 shows longitude-pressure distributions of July mean cooling rates at 20°N and between 40° and 135°E from Katayama's study, and from the present study for both 1984 and 1987. Katayama's calculations show maximum cooling at 400 mb ($\sim$3°C day^{-1}) between 70° and 120°E. In this study, maximum cooling of the same magnitude is found around 300 mb. The difference in location is due to differing cloud specification between the two studies. In Katayama's calculations, clouds were incorporated climatologically with cloud levels assigned to the nearest model level. In our calculations, cloud-top and cloud-base levels are not necessarily specified at the standard model levels. Cooling rates between 40° and 60°E provided by Katayama are 1.0°–1.5°C day^{-1} larger in the very lowest tropospheric layers, compared to our calculations. These differences arise because our calculations consider water vapor continuum absorption, which suppresses radiative cooling.

Finally, several tests have been carried out to assess sensitivity of the cooling rate profiles to the specified input parameters. For example, Fig. 2a provides vertical distributions of net flux and cooling rate between the surface and 100 mb for a 5° $\times$ 5° grid located over the Arabian Sea (centered at 15°N, 65°E); this is the control case in which the retrieved cloud properties, according to the procedures described above, are used to specify low, middle, and high cloud tops and bases. Figures 2b–f provide the sensitivity responses of the flux and cooling rate profiles to a number of factors, such as (Fig. 2b) skin temperature jump being set to zero; (Fig. 2c) cirrus cloud amount being set to zero; (Fig. 2d) middle and high cloud amounts distributed such that 75% of cloud bases are at LCL, while 25% are at 100 mb below cloud top; (Fig. 2e) same as Fig. 2d but reversing the percentages; and (Fig. 2f) thin clouds assigned bases at 50 mb instead of 100 mb below cloud top. It is clear that in the first five cases, net fluxes and cooling rate variations are quite small (less than 5 W m^{-2} in fluxes and fractions of a degree in cooling rates). This is so at all atmospheric levels, except for Fig. 2b in which the effect of the skin temperature jump on the fluxes and cooling rates in the lowest layers is significant. Even for Fig. 2f, where thin clouds are 50 mb thick instead of 100 mb, the changes in net flux in the cloud layers compared to Fig. 2a are less than 10% (between 5 and 15 W m^{-2}). The corresponding cooling rates differences are measurable but small. Nevertheless, for all six cases, total atmospheric cooling remains unchanged since the clouds are effectively optically thick (see Table 3).

The above tests demonstrate that vertical cooling rate profiles are sensitive to specification of cloud base, especially when large amounts of thin clouds are present. However, since cloud-base information is difficult to obtain over oceans, modeling and observationally based studies use simplifying assumptions about cloud-base distributions (see Morcrette 1990; Slingo and Slingo 1988; Ackerman and Cox 1987; Frouin et al. 1988). As discussed below, cooling rate profiles in the monsoon region are predominantly controlled by cooling near cloud top, since large amounts of clouds are of the convective type with bases near the lifting condensation levels.

4. Results

The main results of the radiative cooling analysis are presented in this section, whereas the following section

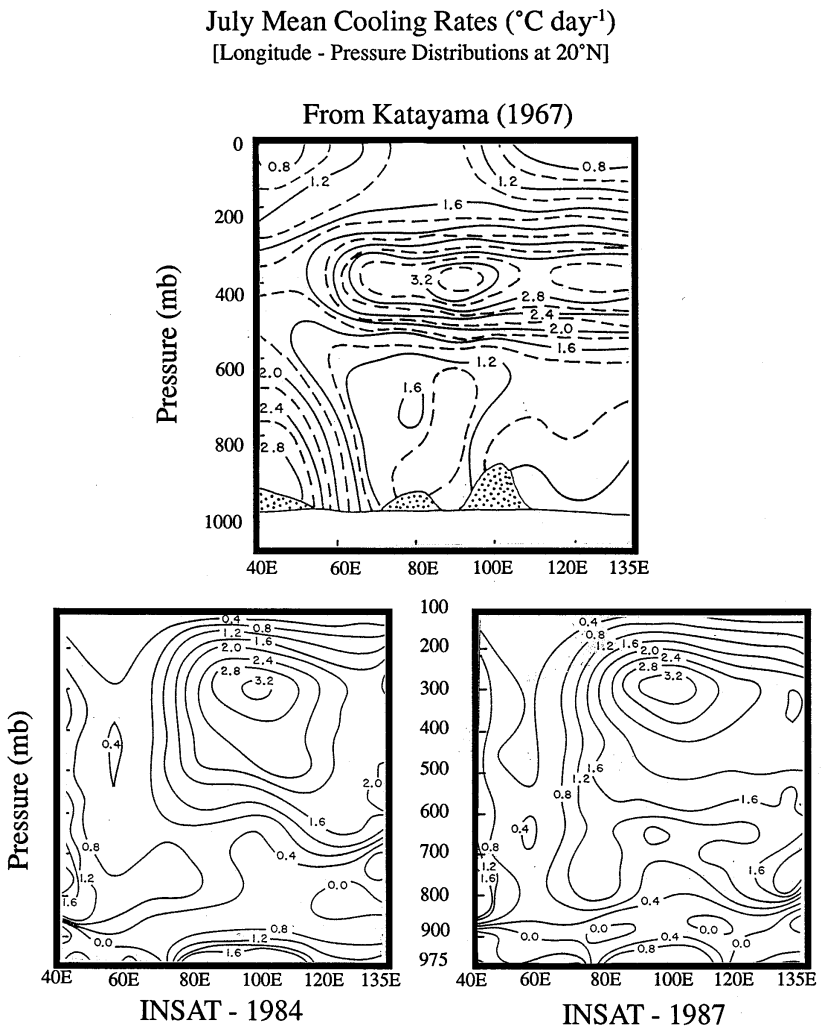

FIG. 1. Longitude–pressure distributions of July mean cooling rates (°C day^{-1}) at 20°N from Katayama's (1967) study (top), and from present study for 1984 (bottom left) and 1987 (bottom right). Contour intervals are 0.2, 0.4, and 0.4°C day^{-1}, respectively.

examines possible effects of radiative cooling variability on intraseasonal wave behavior. For both monsoon seasons, cooling rates are modulated primarily by cloud distributions, and although the general nature of the cloud and cooling rate distributions are similar during the two years, there are important quantitative differences.

a. Seasonal mean cloudiness distributions

Spatial distributions of seasonal mean total cloud amount for 1984 and 1987 are shown in the top two panels of Fig. 3a. For comparison, seasonal mean cloud amounts from the *Nimbus-7* climatology for the 1979–84 period are also shown in the bottom panels. As mentioned, cloud amounts are stratified into low, middle, high, and cirrus categories. The vertical distribution of INSAT-derived cloud amounts during 1984 is shown in Fig. 3b without the associated *Nimbus-7* fields.

The two figures reveal two domains to the east and west of approximately 60°E, over which the cloud amounts and distribution patterns are clearly different. To the east of the 60°E meridian, over the central and eastern Indian Ocean, the Bay of Bengal, the Indian subcontinent, the Maritime Continent, and the western Pacific Ocean, mean cloud amounts are as large as 60%–80%. Most clouds over these regions are in the middle and high categories (see panels 2 and 3 of Fig. 3b). Middle cloud amounts range from 30%–45%, whereas high cloud amounts are between 10% and 30% over the Indian Ocean and between 40% and 60% over the western Pacific Ocean. According to the retrieval scheme, cirrus is most prevalent over regions where middle and high cloud amounts are large. Maximum cirrus amounts,

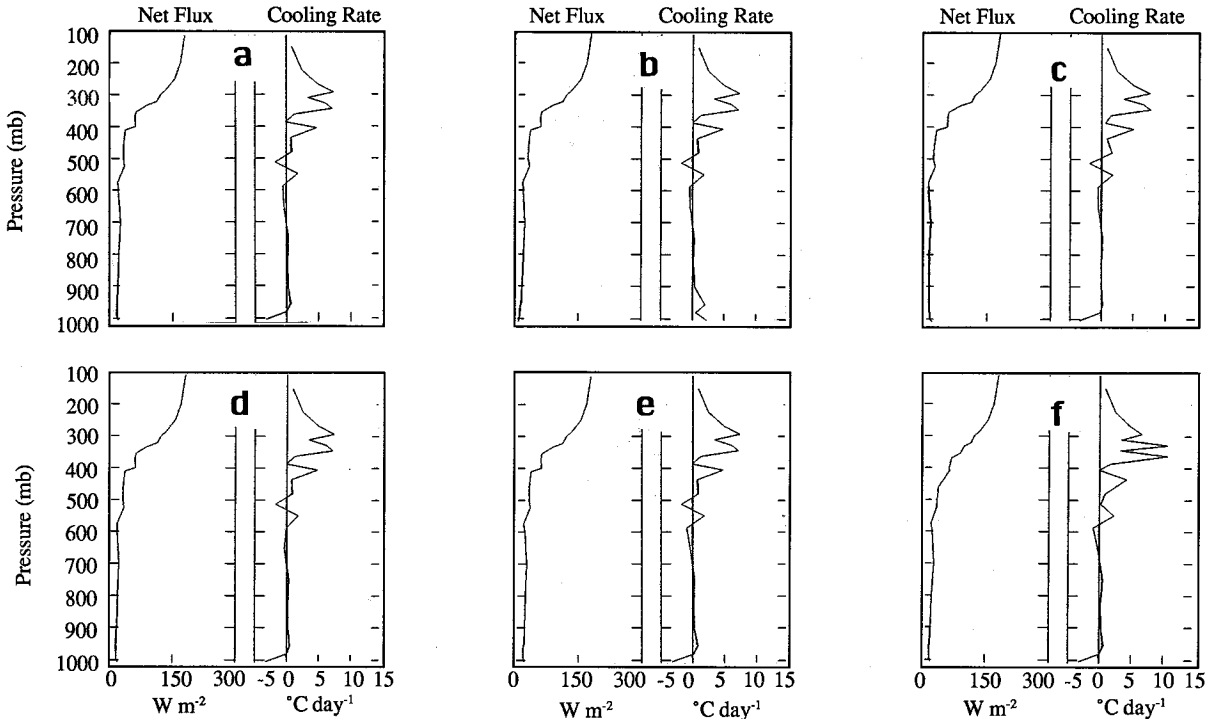

FIG. 2. Vertical profiles of net infrared fluxes (W m^{-2}) and cooling rates (°C day^{-1}) between surface and 100 mb over the Arabian Sea (grid centered at 15°N, 65°E) for six different cases: (a) control calculations, (b) zero skin temperature jump, (c) cirrus amount set to zero, (d) 75% of middle and high cloud specified as ''thick'' and 25% as ''thin,'' (e) 25% of middle and high cloud specified as thick and 75% as thin, and (f) cloud base specified 50 mb below cloud top.

on the order of 10%–12%, are found over the Bay of Bengal and the western Pacific Ocean. On the other hand, to the west of 60°E, over the western Arabian Sea, the western Indian Ocean, the Arabian Peninsula, and the central Asian region, cloud amounts range between 20% and 50%. As seen in the top panel of Fig. 3b, these regions consist of primarily low and middle cloud.

In general, seasonal mean cloud amounts derived from the INSAT measurements compare well with those from *Nimbus-7* (Fig. 3a). In particular, over oceanic regions where most clouds are in the middle and high categories, the differences are minor. On the other hand, over the western Indian Ocean, the Arabian Peninsula, the central Asian region, and the central and western Indian subcontinent, the INSAT-derived cloud amounts are 10%–15% higher than those of *Nimbus-7*, mostly related to the low cloud category. A number of factors can give rise to such differences. Some differences stem from comparing a one-year realization to a six-year climatological mean. Also, different threshold temperatures are used to detect clouds, for example, the INSAT EBBT's 6°C threshold versus a variable threshold for the *Nimbus-7* algorithm (although over the ocean the threshold is generally close to 6°C). Finally, the spatial resolution of the INSAT measurements (22 km) is effectively higher than the set of measurements that determine the spatial resolution of the *Nimbus-7* retrievals. The latter retrievals are based on measurements from the 11.5 μm channel on the Temperature–Humidity Infrared Radiometer, whose ground resolution extends from 6.7 to ~25 km across a scan, and from the 0.36/0.38 μm channel measurements from the Total Ozone Mapping Spectrometer, whose ground resolutions extend from 50 to ~200 km across a scan. All these factors give rise to differences in the retrievals. Moreover, cloud retrievals from INSAT are based only on 12 UTC images, whereas *Nimbus-7* cloud amounts are based on averages from a combination of near-noon and near-midnight local time measurements. Diurnal variability may be the cause of these differences, which show up mostly in the low cloud amounts, although current ISCCP analysis has not refined diurnal effects to the point we can be certain of this; see Rossow et al. (1993).

TABLE 3. Total tropospheric cooling rates for six different sensitivity cases shown in Fig. 2.

Test case	Total tropospheric cooling rates (°C day^{-1})
(a) Control calculations	1.46
(b) Zero skin temperature jump	1.56
(c) Cirrus amount set to zero	1.48
(d) 75% thick clouds, 25% thin clouds	1.46
(e) 25% thick clouds, 75% thin clouds	1.45
(f) ΔP = 50 mb for thin clouds	1.45

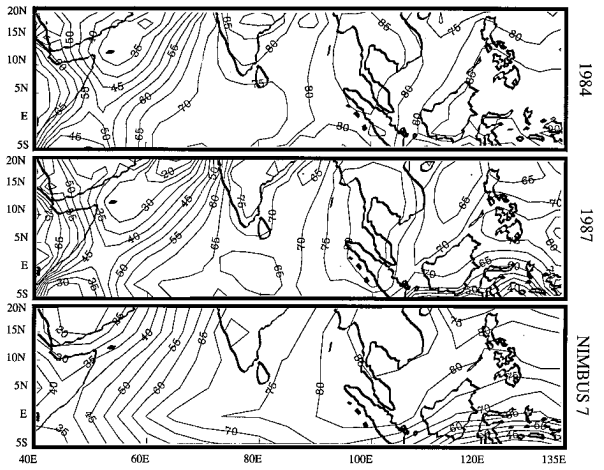

FIG. 3a. Spatial distributions of seasonal mean total cloud amount from INSAT-1984 (top), INSAT-1987 (middle), and *Nimbus-7* cloud climatology (bottom). Units are in percent; contour interval is 5%.

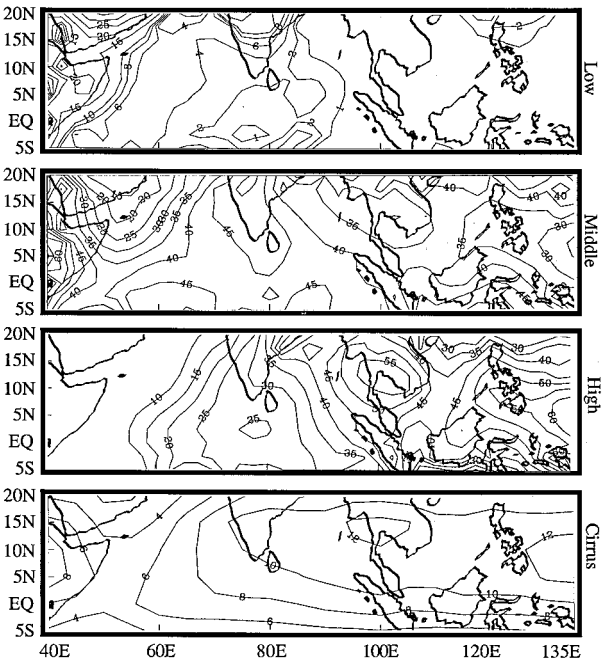

FIG. 3b. Spatial distributions of seasonal mean low, middle, high, and cirrus cloud amounts obtained from INSAT-1984. Units are in percent; contour intervals are 5% for middle and high cloud amounts, and 2% for low and cirrus cloud amounts.

A key feature, seen in Fig. 3a, is that although the spatial distributions of cloud amount are similar between the 2 years, seasonal mean cloud amounts are larger by 5%–10% during 1984. Maximum differences of ~20% are found over the Arabian Sea and the equatorial western Pacific Ocean. Over the Indian monsoon region, differences are primarily in low and middle cloud categories. As noted, 1984 was a normal rainfall season over the Indian monsoon, whereas 1987 was a drought year. Apparently, differences in low and middle cloud amounts reflect differences in regional scale monsoon activity, although large-scale controls are similar. Over the western Pacific Ocean and the South China Sea, differences are primarily in the middle and high clouds. This may be related to interannual variability of sea surface temperature in the Pacific Ocean. For example, a major El Niño–Southern Oscillation (ENSO) occurred during 1987 (Arkin 1988). The normal center of tropical convection during an active ENSO shifts eastward toward the central Pacific with more subsidence associated with the displaced Walker circulation suppressing convection over the western Pacific. The smaller middle and high cloud covers during 1987 are due to that shift in the tropical zonal circulation.

b. Seasonal mean radiative cooling rates

Horizontal and vertical distributions of seasonal mean cooling rate during 1984 are provided in Fig. 4a. Maximum values are found in the upper troposphere at the 300–400 mb levels over the central and eastern Indian Ocean and western Pacific Ocean. Upper-tropospheric cooling rates over these regions are between 3° and 5°C day^{-1}, while midtropospheric (500–700 mb) cooling rates are between 1° and 3°C day^{-1}. Over the western Indian Ocean, the African continent, and the Arabian Peninsula, cooling rates vary between 2° and 4°C day^{-1}, but are relatively uniform above 700 mb.

The cooling rates are obtained by a linear combination of contributions from the cloud-free and cloud-covered areas. Therefore, the cooling rate profile at any (x, y, p) grid location and time t can be written as

$$\mathrm{CR}_{\mathrm{tot}}(x,y,p,t) = [1 - A_c(x,y,t)]\mathrm{CR}_{\mathrm{clr}}(x,y,p,t) + \sum_{i=1}^{M} [A_{c,i}(x,y,t)\mathrm{CR}_{\mathrm{cld},i}(x,y,p,t)], \quad (1)$$

where $\mathrm{CR}_{\mathrm{tot}}$ is the total cooling rate, $\mathrm{CR}_{\mathrm{clr}}$ and $\mathrm{CR}_{\mathrm{cld}}$ are the cooling rates from cloud-free and cloudy portions, A_c is total cloud amount, and the $A_{c,i}$'s are cloud amounts in various cloud-top categories. Thus, the cooling rate distribution shown in Fig. 4a is obtained from seasonal mean cloud-free and cloud-induced components. These latter quantities are shown in the left and right panels of Fig. 4b.

What stands out in this diagram is that over the central–eastern Indian Ocean and western Pacific Ocean areas, cooling rates are primarily cloud induced. The cloud-free cooling rates over these regions are as small as ~0.5°C day^{-1}. On the other hand, over the western Indian Ocean, east Africa, and the Arabian Peninsula, contributions from cloud-free and cloud-induced cooling rates are of equal magnitude (1°–2°C day^{-1}). The cooling rates are minimum between 850 and 950 mb at ~0.5°–2.0°C day^{-1}. At the lower levels, cooling rates are primarily determined by the combination of cloud-base height and water vapor mixing ratio factors.

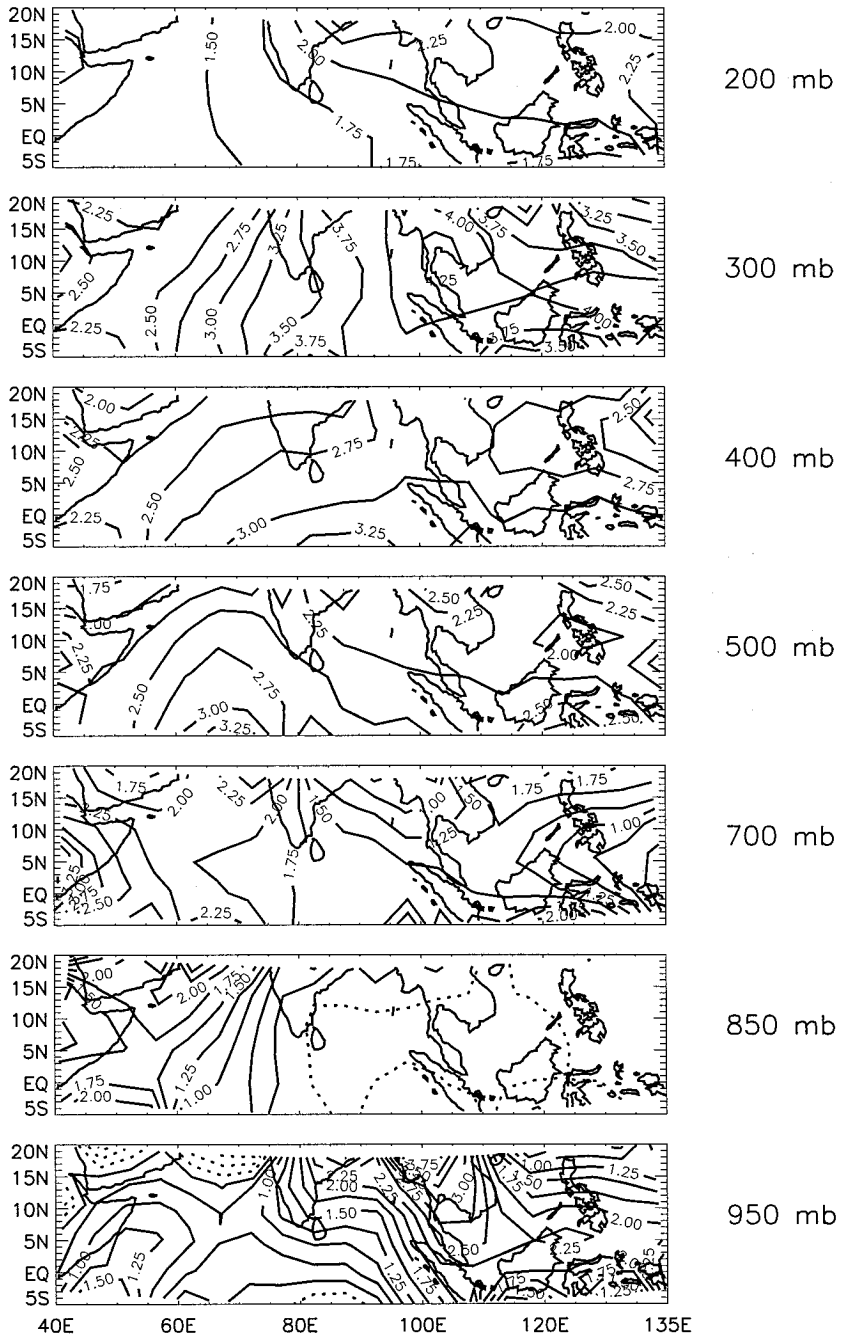

FIG. 4a. Vertical distribution of seasonal mean cooling rates between 5°S–20°N and 40°–135°E for 1984. Units are in °C day^{-1}.

The distributions of seasonal mean cooling rate are consistent with the cloud distributions discussed in the previous section. Maximum cooling rates are found at 300–400 mb over the Indian and western Pacific Oceans where middle and high cloud amounts are large. To the west of 60°E, where clouds are mostly confined to the lower and middle troposphere, maximum cooling rates are consistently found in the lower troposphere at 700 mb. The maximum cooling rates appear to be related to cloud tops with cooling below the tops suppressed.

A comparison of seasonal mean cooling rates during 1984 and 1987 shows that the spatial distributions are qualitatively similar. The magnitudes of cooling show small differences related to differences in low and middle cloud amounts, distributions of boundary layer moisture, and the organization of synoptic-scale sys-

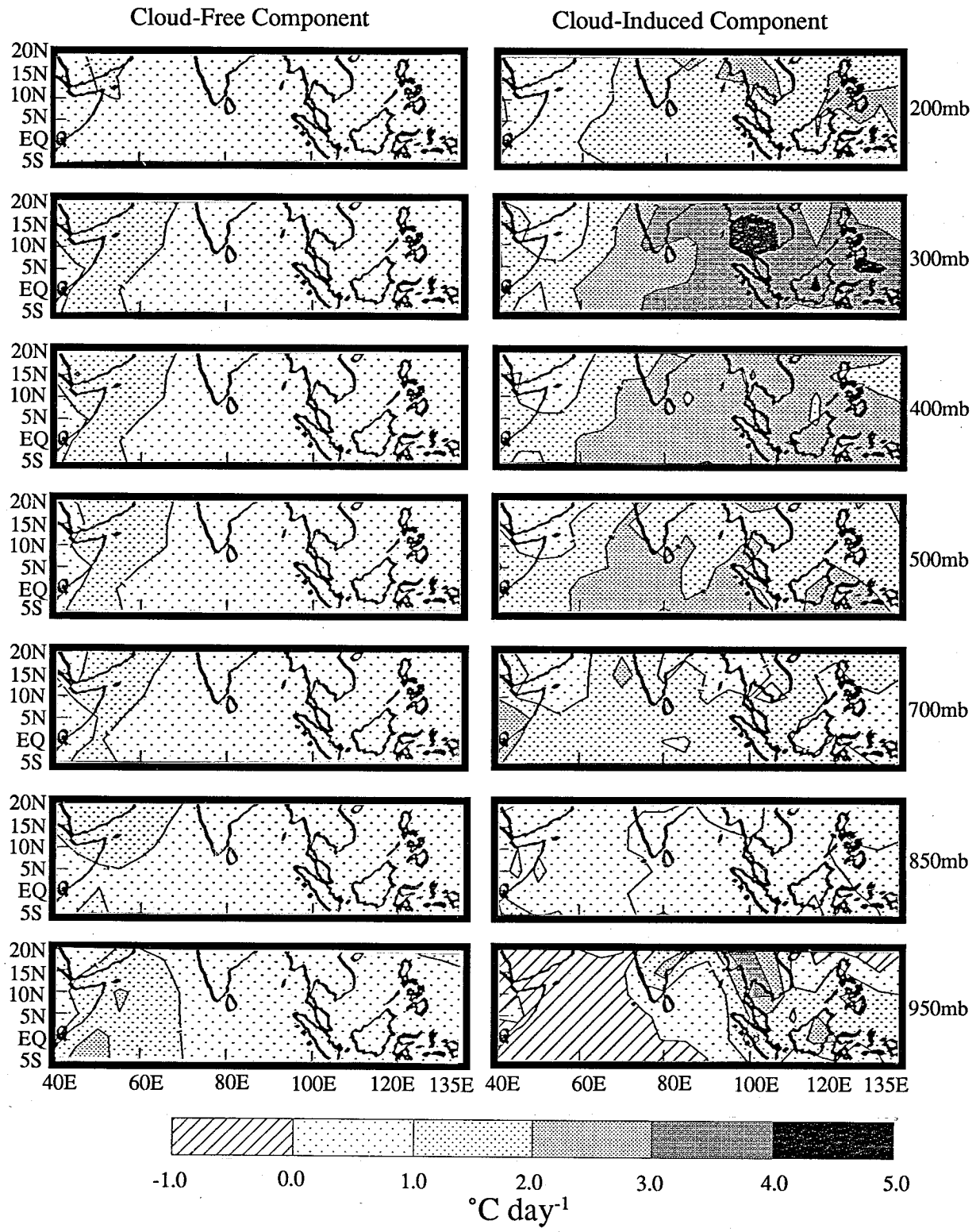

FIG. 4b. Same as Fig. 4a except for cloud-free and cloud-induced components of cooling rates.

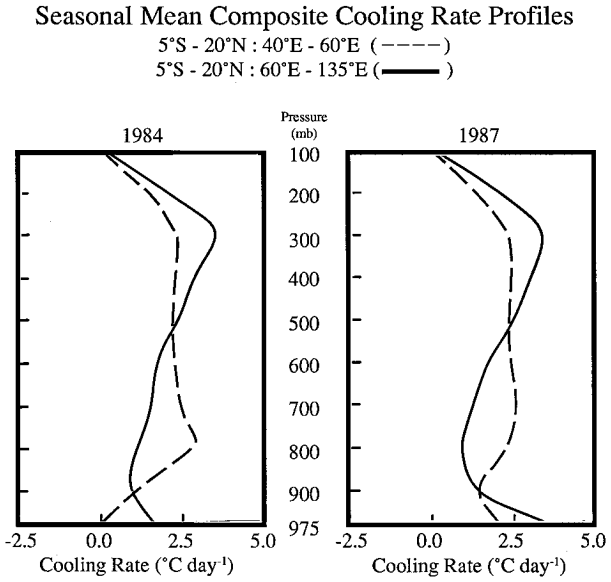

FIG. 5. Seasonal mean cooling rate profiles spatially averaged over 5°S–20°N and 60°–135°E (solid line), and over 5°S–20°N and 40°–60°E (dashed line) during 1984 (left) and 1987 (right). Units are in °C day^{-1}.

tems. This is illustrated in Fig. 5, which shows seasonal mean cooling rate profiles spatially averaged between 5°S–20°N and 60°–135°E (shown as solid lines), and between 5°S–20°N and 40°–60°E (shown as dashed lines). The averaged cooling rate profiles east of 60°E exhibit maximum cooling rates of 4°C day^{-1} near 300 mb, decreasing above and below this level during both years. The cooling rates have a minimum value of ~1°C day^{-1} around 800–850 mb. Near the surface, cooling rates increase to 1.5°C day^{-1} during 1984 and to 3.0°C day^{-1} during 1987. The averaged profiles west of 60°E show almost constant cooling of ~2°C day^{-1} between 300 and 800 mb during 1984 and ~2.5°C day^{-1} during 1987.

The cooling rate profiles shown here represent layer cooling. Clouds cool atmospheric layers locally near cloud tops, but suppress atmospheric cooling to space by 0.2°–0.5°C day^{-1} over several oceanic regions where large amounts of high cloud are present. The seasonal mean cooling rate profiles found over most of the Indian and western Pacific Oceans have a common feature with the profiles obtained by Katayama (1967) and Dopplick (1972) in that large cooling rates are found in the upper troposphere. However, in contrast to our calculations, the vertical levels of maximum cooling in these two studies are found between 300 and 450 mb, related to differences in how cloud-top heights are specified.

c. Intraseasonal variability of cloudiness

As noted, cloud distribution exerts the dominating influence on the magnitude and distribution of cooling rates. Therefore, it is worthwhile to examine the intra-

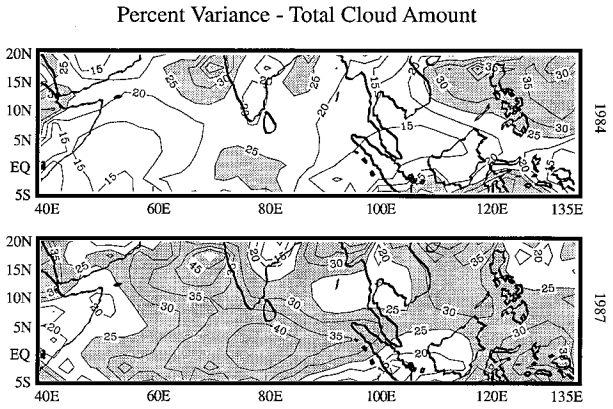

FIG. 6a. Spatial distributions of percentage of cumulative variance of total cloud amount (contained within 21–76-day intraseasonal bandpass) during 1984 (top) and 1987 (bottom). Contour interval is 5%, and shaded areas indicate percentage variances greater than 25%.

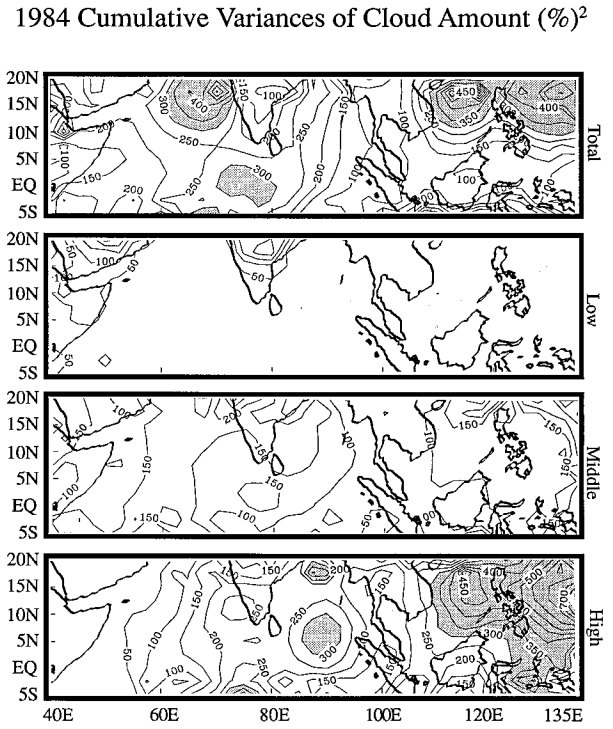

FIG. 6b. Spatial distributions of cumulative variance for total, low, middle, and high cloud amounts (in 21–76-day bandpass) during 1984. Contour interval is 50%^{2}, and shaded areas indicate cumulative variances greater than 300%^{2}.

seasonal variability of cloudiness itself before examining intraseasonal variability of the radiative cooling process. The cloud amounts are first filtered to extract intraseasonal frequencies with periods between 21 and 76 days. This bandpass is associated with discrete Fourier frequencies of the 152-day time series used in the analysis. Although this frequency band is broader than used in some of the prior studies (20–60 or 30–50 days),

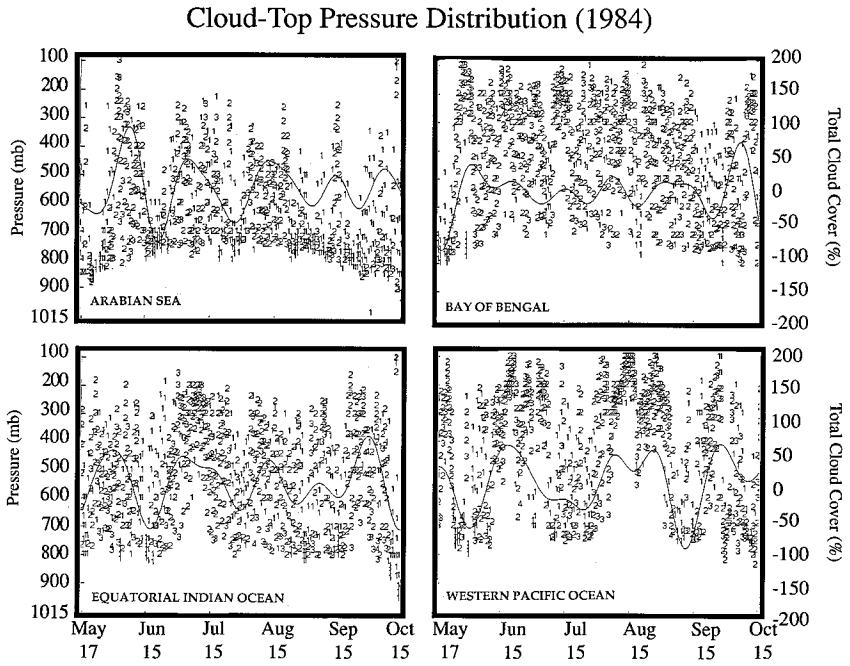

FIG. 7. Time series of cloud-top pressure distributions during 1984 for grid centered over the Arabian Sea, Bay of Bengal, equatorial Indian Ocean, and western Pacific Ocean. In diagrams, 1 indicates cloud amount between 1% and 10%, 2 between 11% and 20%, 3 between 21% and 30%, etc. The smooth line shows 21–76-day bandpass filtered total cloud amount.

Weickmann et al. (1985) have shown that the properties of intraseasonal phenomena remain robust within this band.

Figure 6a shows spatial distributions of intraseasonal percentage variance of total cloud amount during 1984 and 1987 for the 21–76-day bandpass. During both seasons, the centers of largest intraseasonal variance (>25%) are found over the equatorial Indian Ocean, the Arabian Sea, the Bay of Bengal, and the western Pacific Ocean. Notably, the spatial distributions of variance are very similar during both seasons. However, over oceanic centers, percentage variances during 1987 are larger by 10–15% compared to those during 1984. Moreover, over these centers, intraseasonal variability primarily stems from middle and high clouds. This is shown in Fig. 6b, which provides spatial distributions of variance in the 21–76-day bandpass for total, low, middle, and high cloud amounts during 1984. The variances in total cloud amount over the oceanic centers range between 300% and 450%^{2} (percent squared), corresponding to root-mean-square amplitudes of 15%–21% (top panel of Fig. 6b).

A comparison with the variances in low, middle, and high cloud amounts (lower three panels in Fig. 6b) indicates that the largest variability is in high cloud amount, that is, clouds with tops above 7 km. Over the equatorial Indian Ocean, the Bay of Bengal, and the western Pacific Ocean, high clouds exhibit variances of 250%^{2}–700%^{2}, corresponding to root-mean-square amplitudes of about 15%–25%. Middle clouds, with cloud tops between 2 and 7 km, exhibit variances of ~150%^{2} over the Arabian Sea, the equatorial Indian Ocean, and the western Pacific Ocean, corresponding to root-mean-square amplitudes of ~12%. Low clouds, which are mostly confined to the land regions of the Arabian Peninsula and central India, exhibit the smallest variances of ~100%^{2}, corresponding to root-mean-square amplitudes of ~10%.

It is evident from the variance distributions that the largest intraseasonal variability is in the middle and high cloud categories. This is further shown in Fig. 7, which provides time series of cloud-top pressure distribution over the Arabian Sea, the Bay of Bengal, the equatorial Indian Ocean, and the western Pacific Ocean. The values in the diagrams indicate cloud amounts and cloud-top locations. A bandpass filtered time series of total cloud amount for each region is also shown as a continuous line in each of the diagrams. It is clear that there are distinct episodes of elevated and depressed cloudiness on intraseasonal timescales. In particular, clouds with tops above 400 mb undergo periodic changes related to cycles of enhanced and suppressed deep convection. This is consistent with the findings of Lau and Chan (1986), Knutson and Weickmann (1987), and Smith and Mehta (1990), studies noting that intraseasonal variability is a process primarily controlled by deep convection. A point of interest in Fig. 7 is that the time periods between enhanced and suppressed episodes are quite different from one region to another, indicating the broadband nature of intraseasonal variability. As

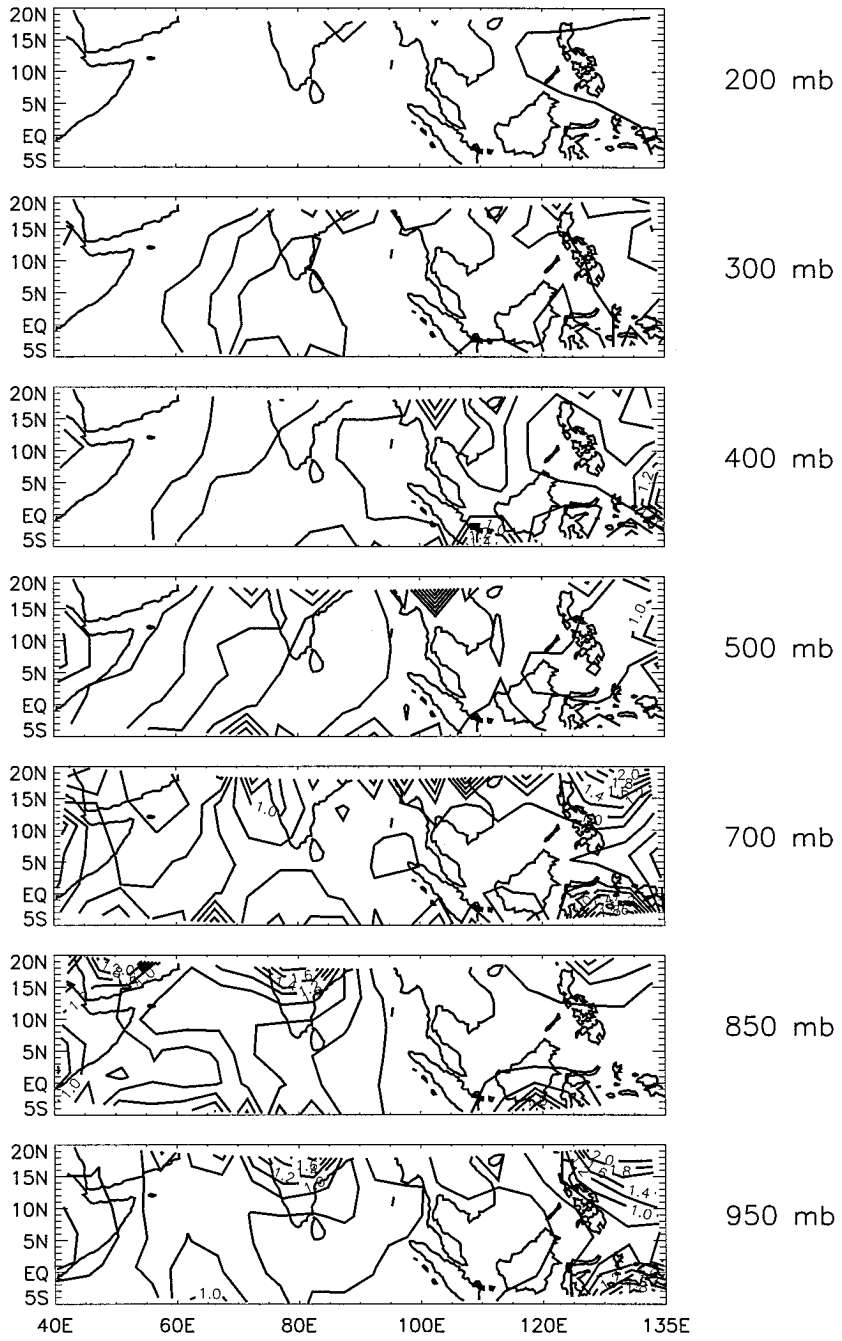

FIG. 8a. Vertical distribution of cumulative variance of cooling rates between 5°S–20°N and 40°–135°E (in 21–76-day bandpass) for 1984. Units are in 10 (°C day^{-1})^2.

pointed out in the following, such periodic bursts in deep convection strongly modulates the radiative cooling rate profiles.

d. Intraseasonal variability of radiative cooling rates

Analogous to cloud amounts, intraseasonal analysis of the radiative cooling rates is accomplished by isolating variations in the 21–76-day bandpass from the cooling rate time series. It can be shown that Eq. (1) holds for the filtered time series of total, cloud-free, and cloud-induced cooling rates, since the same filter is used on all three time series. Rewriting Eq. (1) as

$$A(x, y, p, t) = B(x, y, p, t) + C(x, y, p, t), \quad (2)$$

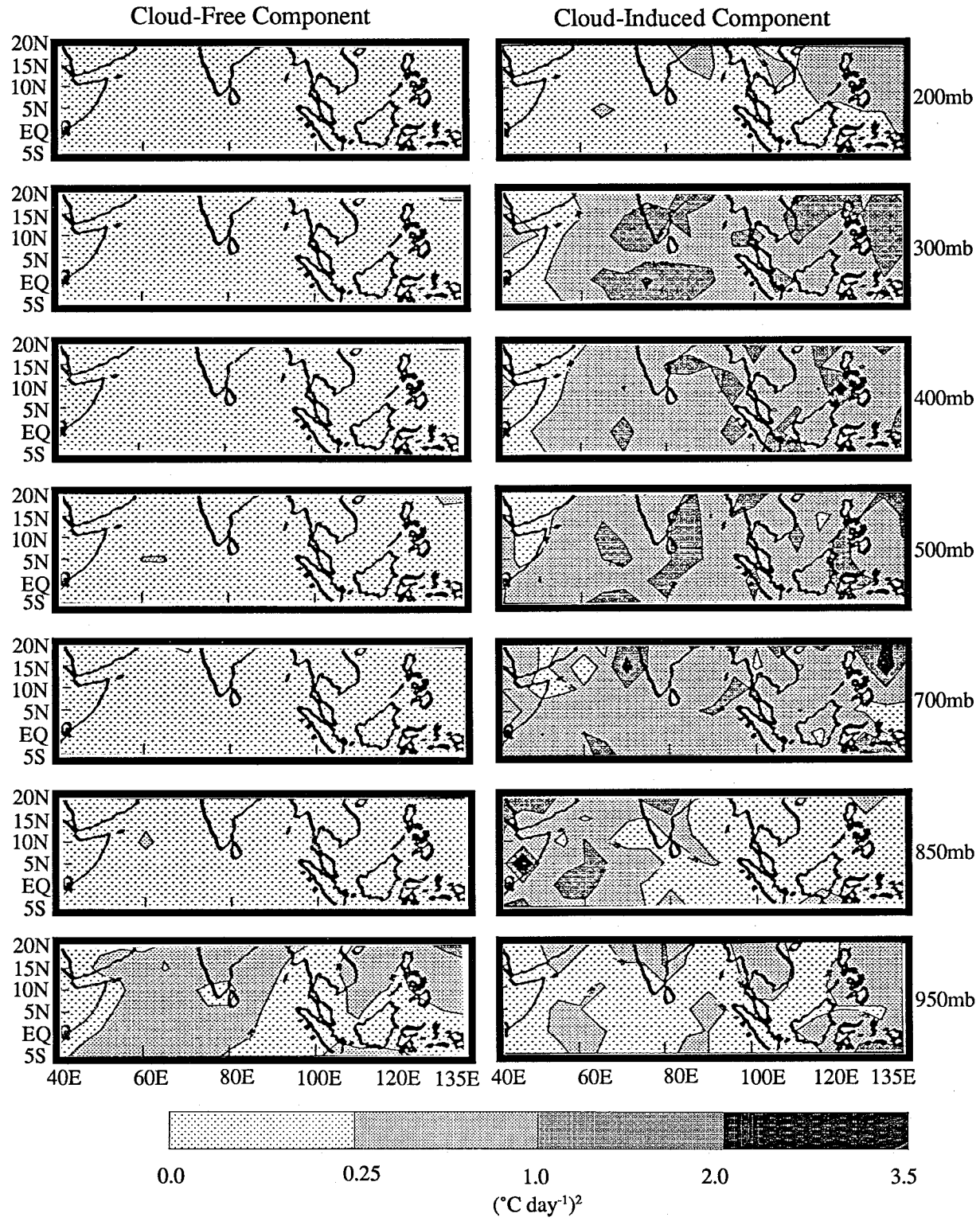

FIG. 8b. Same as Fig. 8a except for cloud-free and cloud-induced components.

the cumulative variance of cooling rate within the intraseasonal band can be written as

$$A_V(x, y, p) = B_V(x, y, p) + C_V(x, y, p) + 2\overline{B'C'}, \quad (3)$$

where A_v, B_v, and C_v are the variances in total, cloud-free, and cloud-induced cooling rates for the filtered time series, and $\overline{B'C'}$ is the covariance between cloud-free and cloud-induced cooling rates.

Spatial distribution of cumulative variance in total cooling rate (A_v) during 1984 is shown in Fig. 8a. Distributions of B_v and C_v are shown in Fig. 8b. It is evident that the largest variances are found in the cloud-induced cooling rates (right panel of Fig. 8b). This is not surprising since cloudiness itself shows strong intraseasonal variability. Consistent with this variability, the centers of maximum variance in cooling rate are also found over the central equatorial Indian Ocean, the Arabian Sea, the Bay of Bengal, the South China Sea, and the western Pacific Ocean. Moreover, the peak variances of these centers are found between 300 and 400 mb, indicating the influence of middle and high cloud variability. The variances in cloud-induced cooling rates within the above-mentioned centers range from 1.0 to 2.5(°C day^{-1})^2 corresponding to root-mean-square cooling rate amplitudes of 1.0°–1.5°C day^{-1}. Similarly, over the western Indian Ocean, variances are also between 1.0 and 2.5(°C day^{-1})^2 except that maximum variances are found in the lower troposphere, related to variability of low and middle clouds.

On the other hand, the cloud-free component over most of the domain (left panel of Fig. 8b) exhibits smaller variances ~0.2(°C day^{-1})^2, representing root-mean-square amplitudes of ~0.5°C day^{-1}. At 950 mb, however, the variance in the cloud-free component is between 0.25 and 1.0(°C day^{-1})^2, which is related to the variability of boundary layer moisture. The covariances between cloudy and cloud-free cooling rates (not shown) are between −0.2 and 0.2(°C day^{-1})^2 everywhere, except over the Indian Ocean at 300 mb, where they are about −1(°C day^{-1})^2. The combination of these cloud-free and cloud-induced terms results in the intraseasonal variances of total cooling rates shown in Fig. 8a.

A comparison of cooling rate variability between 1984 and 1987 is shown in terms of composite cooling rates over four selected regions, where intraseasonal variances are maximum. These regions are shown in Fig. 9: 1) equatorial Indian Ocean (5°S–5°N, 60°–90°E); 2) Maritime Continent and equatorial western Pacific Ocean (5°S–5°N, 100°–130°E); 3) Arabian Sea, Bay of Bengal, and Indian subcontinent (10°–20°N, 60°–90°E); and 4) southeast Asia, South China Sea, and western Pacific Ocean (10°–20°N, 100°–130°E). Figure 10a shows time–pressure distributions of spatially averaged cooling rates over region 1 during 1984 and 1987. Diagrams in the left panel show total cooling while those in the right panel show 21–76-day bandpass filtered cooling (referred to as intraseasonal anomalies). During

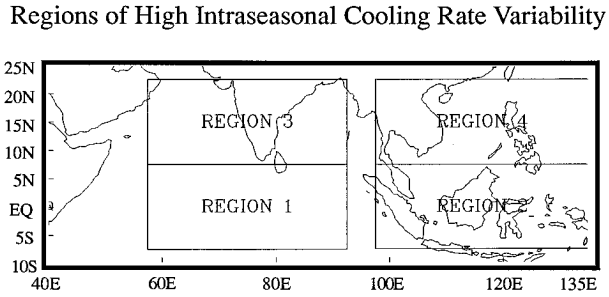

FIG. 9. Geographical locations of the regions of large intraseasonal variances. The regions are 1) equatorial Indian Ocean (5°S–5°N/60°–90°E); 2) Maritime Continent and equatorial western Pacific Ocean (5°S–5°N/100°–130°E); 3) Arabian Sea, Bay of Bengal, and Indian subcontinent (10°–20°N/60°–90°E); and 4) Southeast Asia, South China Sea, and western Pacific Ocean (10°–20°N, 100°–130°E).

both seasons, total cooling rates between 250 and 400 mb become periodically enhanced to 3.0°–4.5°C day^{-1}. At the same time, cooling rates below 400 mb are suppressed. This pattern is more noticeable in the cooling rate anomaly distributions, which show that the upper and lower troposphere experience out-of-phase radiative cooling rate anomalies, with anomalies generally between 0.25°–1.0°C day^{-1}. This is the case over all four regions shown in Fig. 9. As an example, time–pressure distributions of the anomalies over regions 2, 3, and 4 for 1984 and 1987 are shown in Fig. 10b. Of note is that during 1987, the amplitudes of the anomalies are 10%–15% larger, as compared to 1984, over the Indian Ocean, the Arabian Sea, and the Bay of Bengal regions (region 1 and 3 in Figs. 10a,b). These are the regions where cloud amounts also exhibit the strongest intraseasonal amplitudes during 1987 (Fig. 6a).

It is clear that the intraseasonal variability of cooling rates is primarily cloud induced. Previous studies of satellite-based investigations have shown intraseasonal variability of cloudiness and OLR, which provide top-of-atmosphere perspectives of the variability. What stands out in this analysis is that radiative cooling rates have a continually changing vertical structure related to the intraseasonal variability of cloud distribution. Recalling the nature of cloud-top variability (Fig. 7), it is evident that cooling rates are modulated by episodes of enhanced and suppressed deep convection. When deep convection is present, cloud-top cooling enhances upper tropospheric cooling rates, whereas below cloud tops, cooling is suppressed. When deep convection is not present, upper tropospheric cooling rates are reduced, and maximum cooling rates shift to the middle troposphere related to the cloud-top heights of low and middle clouds. The nature of the cooling rate profiles found here is qualitatively similar to that found by Cox and Griffith (1979b) based on GATE measurements. They calculated composite cooling rate profiles for convectively disturbed and undisturbed conditions, showing similar effects of deep convective clouds on the cooling rate profiles. Ackerman and Cox (1987) also pointed

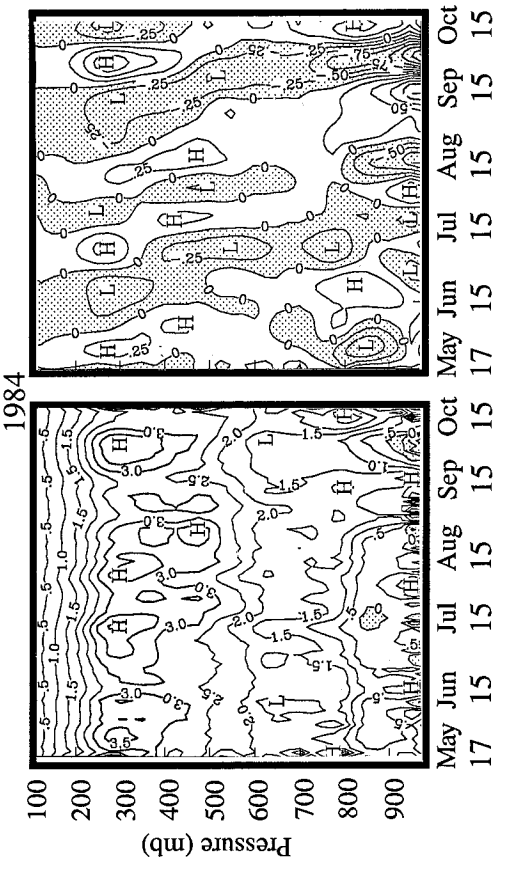

FIG. 10a. Time series of cooling rate profiles (left panels) and 21–76-day bandpass filtered cooling rate profiles (right panels) during 1984 (top panels) and 1987 (bottom panels). The cooling rates are spatially averaged over the equatorial Indian Ocean region 1 shown in Fig. 9. Contour intervals are 0.5°C day^{-1} for the total cooling rates and 0.25°C day^{-1} for the filtered anomalies.

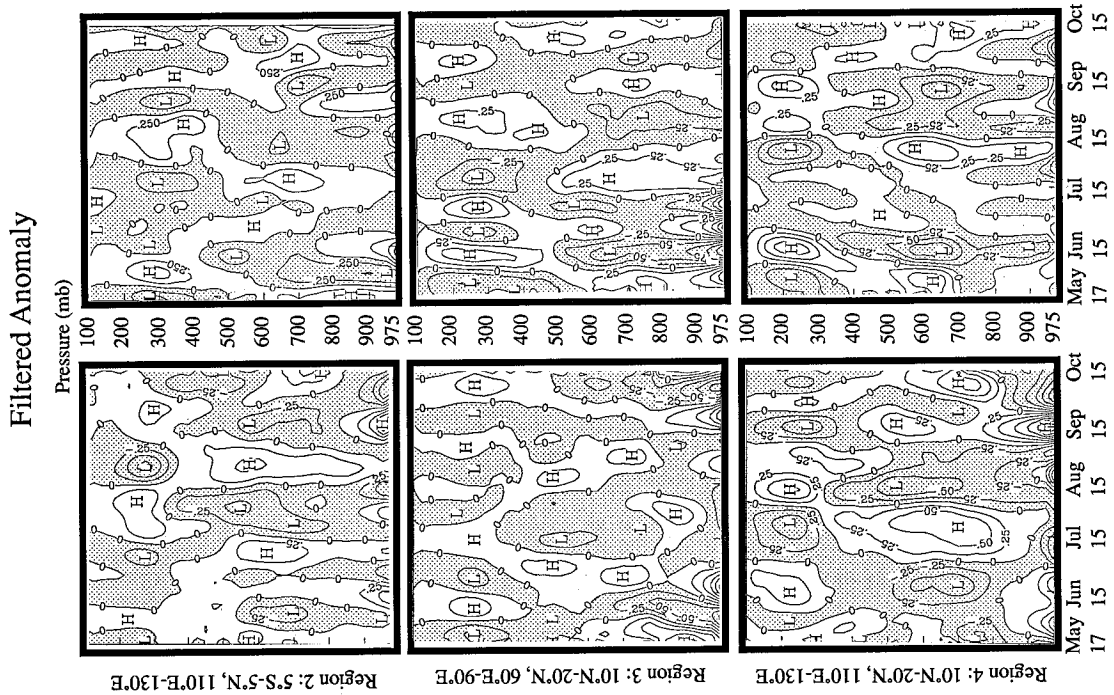

FIG. 10b. Time series of 21–76-day bandpass filtered cooling rate profiles during 1984 (left panels) and 1987 (right panels). The cooling rates anomalies are for regions 2, 3, and 4 shown in Fig. 9. Contour interval is 0.25°C day^{-1}.

out similar control of clouds on the cooling rate profiles during various phases of the 1979 summer monsoon. As shown in the following section, relative control of middle and high clouds on the cooling rate anomalies during 1984 and 1987 become more evident when decomposing the anomalies into their vertical modes.

e. Vertical modes of radiative cooling rates

In order to characterize the vertical structure of cooling rates on intraseasonal timescales, principal component analysis is used. The cooling rate anomaly distributions over the four regions shown in Figs. 10a,b are decomposed such that

$$\mathrm{CR}(p, t) = \sum_{n=1}^{N} \mathrm{PC}_n(p)\mathrm{EOF}_n(t), \tag{4}$$

where CR is the pressure–time distribution of cooling rate anomalies, the $\mathrm{PC}_n(p)$ vectors are principal components that provide vertical structure of the cooling rates, and the $\mathrm{EOF}_n(t)$ are basis functions that provide the corresponding anomaly time series; see Legler (1983, 1984) for a discussion of this technique.

The first two vertical modes and their corresponding time series of cooling rate anomalies over the four regions outlined in Fig. 9 are provided in Figs. 11a,b for 1984 (solid lines) and 1987 (dashed lines). The variances described by each mode are also shown. The first two EOFs contain 70%–85% of the total variance. The first mode itself contains 45%–75% of the variance considering all four regions. The structure of the first vertical mode over all four regions is one in which there is one zero crossing between 400 and 500 mb. This mode represents a feature of the intraseasonal cycle in which the upper troposphere experiences sequential positive and negative anomalies that are out of phase with the lower troposphere. In this sense, it captures the basic nature of the profiles shown in Figs. 10a,b, and represents the controls of deep convection on the cooling profiles. The second mode exhibits multiple zero crossings with the middle troposphere out-of-phase with both upper and lower troposphere, related to variations in low and middle cloudiness. The cooling rate variability in these modes is typically between 0.5° and 1.0°C day^{-1}.

Similarities and differences between the two years are evident in Fig. 11. Qualitative similarities in the modes indicate that the large-scale atmospheric controls over cloudiness, moisture, and radiative cooling rates remain the same during the two seasons. However, the first mode exhibits consistently larger variance during 1987, whereas the second mode exhibits larger variance during 1984. These differences are related to the interannual variability of the monsoon. Specifically, during 1987, intraseasonal variability of the high clouds is larger compared to the middle and low clouds, whereas during 1984 the variability of low and middle clouds appears to be larger than high clouds. The cooling rate modes in Fig. 11 illustrate this different control of cloudiness during the two years. Also, the periods of variability from one region to another and from one season to the other are different, confirming that a broad band of timescales is associated with intraseasonal phenomena.

The spatial patterns of cloud and cooling rate variability discussed above for the two years suggest that large-scale, interannual variability of the tropical circulation exerts a primary control on them. The first vertical mode of the anomalies (Fig. 11), in which the out-of-phase anomalies of the upper and lower troposphere vary on intraseasonal timescales, is analogous in nature to zonal wind anomalies noted by Madden and Julian (1971). A similar property in the vertical structure of the velocity potential has been pointed out by Knutson and Weickmann (1987). Thus a question arises concerning how cloud-radiative cooling effects feedback on the intraseasonal circulation. Recalling that previous studies have emphasized the role of the vertical structure of diabatic heating on controlling the phase speed of the waves, it is worthwhile examining the role of cloud-radiation feedbacks. Assuming that the principal source of intraseasonal variations in the Tropics are Kelvin waves forced by convective heating, it is reasonable to expect that radiative cooling processes induced by clouds formed within the wave disturbances modify the convective heating profiles and thus modify the waves.

It is difficult to assess the precise role of radiative cooling in modifying the total diabatic heating profile because observations of diabatic heating over the Tropics, particularly the monsoon region where intraseasonal waves obtain their primary forcing, are scarce. Over the tropical Pacific and Atlantic Oceans, several earlier studies have helped characterize diabatic heating profiles using large-scale diagnostic analysis (Reed and Recker 1971; Yanai et al. 1973; Thompson et al. 1979). Frank and McBride (1989) have estimated heating profiles over the Australian monsoon region. In these studies the heating profiles have been obtained for convective disturbances using budget analyses of rawindsonde data. In diagnosing the total heating profiles, Reed and Recker (1971), Yanai et al. (1973), and Thompson et al. (1979) used the climatological mean radiative profiles from Dopplick (1972). Frank and McBride (1989) used mean radiative profiles calculated for the GATE region by Cox and Griffith (1979b). All of these studies have shown that the convective heating profiles differ significantly between convectively active and inactive periods. Yet variations of radiative cooling due to variations in cloudiness have not been considered in deriving the heating profiles. As noted, radiative cooling rate profiles in the upper and lower troposphere vary significantly during convectively active and inactive periods. Therefore, we seek to assess the significance of these fluctuations on the total heating profile and subsequently on intraseasonal waves.

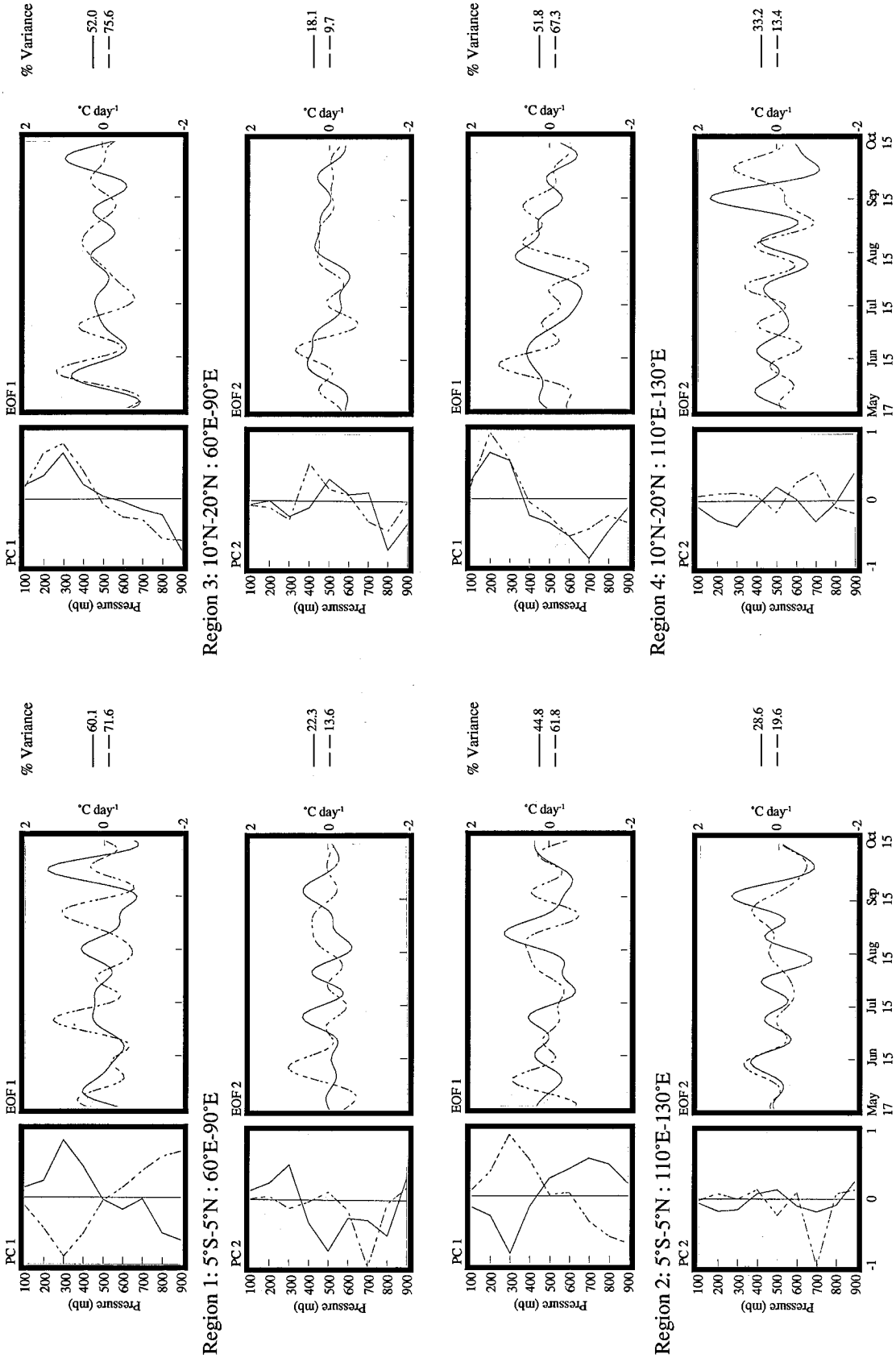

FIG. 11. First two principal components (left) showing vertical modes and their empirical orthogonal function time series (right), based on the time–pressure distributions of the filtered cooling rate anomalies for regions 1, 2, 3, and 4 shown in Fig. 9. Solid lines are for 1984, and dashed lines are for 1987. Percent variances described by each mode are shown to the right of the time series diagrams.

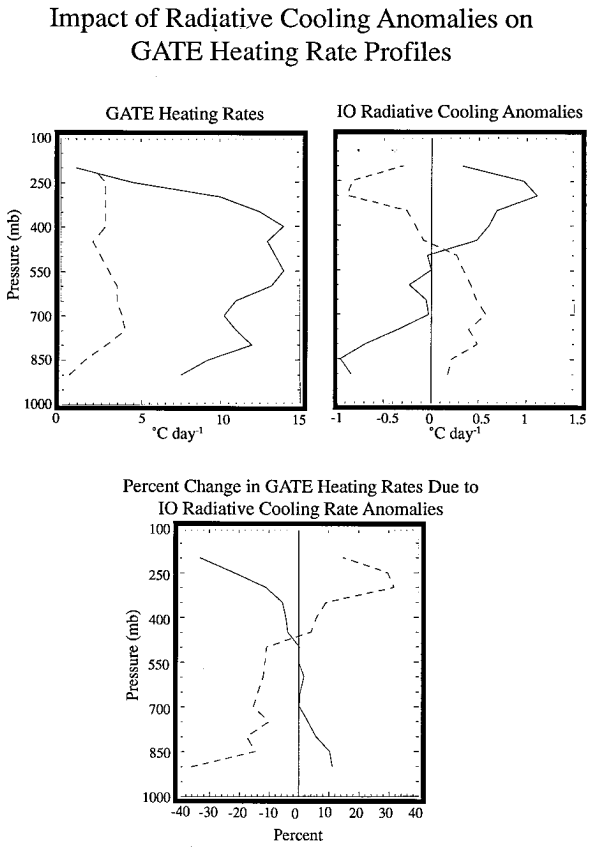

FIG. 12. Upper left panel shows diabatic heating rate profiles for convectively active (solid) and inactive (dashed) phases based on GATE observations. Upper right panel shows radiative cooling rate anomalies composited for same phases over the equatorial Indian Ocean during 1984. Bottom panel shows percent of change in GATE diabatic heating rates due to Indian Ocean radiative cooling rate anomalies during two phases.

To assess how cooling rate variability might modulate the convective heating profile, an example calculation is provided. We begin with the convective heating profiles estimated by Frank and McBride (1989) from their GATE analysis. They considered two extreme phases, one convectively active and the other involving decaying or suppressed convection. Radiative cooling rate anomaly profiles for the two phases are assigned from maximum and minimum anomaly composites of the first and most dominant EOF mode shown in Fig. 11a. As discussed earlier, this mode captures the main features in the variability of radiative cooling rate due to variability of deep convection.

Figure 12 shows the changes in the convective heating profile due to the cooling rate anomalies. The top left panel shows the diabatic heating profiles based on the GATE analysis for active (solid line) and inactive (dashed line) convective conditions. The top right panel shows the radiative cooling rate anomalies for the same two conditions based on the Indian Ocean analysis, while the bottom panel shows the vertically distributed percentage changes in diabatic heating due to the radiative cooling anomalies. It should be emphasized that the GATE profiles taken from Frank and McBride (1989) include mean radiative effects. Therefore, in Fig. 12, extreme changes in radiative cooling are being considered. Figure 12 shows that if variability of the radiative cooling profile over a complete cycle of EOF mode 1 is considered, the resulting convective heating profiles will differ by 2%–30% compared to the original profiles. During an active convection surge, due to radiative cooling near cloud tops, total heating above 450 mb will be reduced up to 30%. At the same time, heating in the lower troposphere will increase from 2% to 10%. During the suppressed phase, total heating in the lower troposphere will decrease by 10%–30% due to the radiative effects of low and middle cloudiness.

Quantitatively, such a comparison would be best carried out with estimates of convective heating profiles obtained over the Indian Ocean. The spatial and temporal scales of the GATE heating profiles and the radiative cooling profiles considered here are somewhat different and so the above example is partly affected by scale mismatch. However, in basic terms, both sets of profiles represent the responses to the same phenomenon, namely, variability of deep convection. Therefore, notwithstanding quantitative precision, the role of radiative cooling in perturbing the convective heating as shown in Fig. 12 is considerable. It can be inferred from the results given in Fig. 12 that the effects of cloud-radiative anomalies are found predominantly in the upper and lower troposphere, where latent heating is least significant. For convective regimes, it is the middle troposphere where latent heating is largest and radiative cooling least; see Houze (1993). This means that perturbative effects of cloud-induced radiative cooling do not necessarily change the fundamental nature of the diabatic heating profile, in that the level of maximum heating remains in the middle troposphere. However, the vertical heating gradient changes episodically due to radiative cooling anomalies, which in turn affects the stability of the troposphere. Thus, perturbations in the vertical heating gradient, due to episodic convective changes governing the environment of a propagating wave, can alter the time period of propagation of the wave, initially excited at a specific frequency by convective heating. In the following section, with the aid of a two-level model of Kelvin waves, we estimate the magnitude of this feedback effect in modulating the phase speed of such waves.

5. Influence of cloud-radiative cooling on Kelvin wave phase speeds

A simple model of equatorial Kelvin waves with first baroclinic mode structure is used to gauge the effect of radiative cooling on the phase speed of planetary-scale

intraseasonal waves. The first baroclinic mode structure is chosen because the dominant mode of the cooling rate anomalies found in this study is similar to such a structure. It is consistent with the observed intraseasonal anomalies of zonal wind and velocity potential (Madden and Julian 1971). There is a rational explanation for the similarity between the vertical cooling rate modes and the model normal modes. In the Indian Ocean–western Pacific Ocean regions, the ocean surface fluxes and low-level convergence exhibit intraseasonal variations (see Krishnamurti et al. 1988; Knutson and Weickmann 1987). These processes affect cloud distributions, which in turn modulate cooling rates. Thus, the vertical modes found in the cooling rate anomalies, which are based on the observed cloudiness, reflect the large-scale dynamical controls on intraseasonal timescale activity. Under these conditions, a Kelvin wave model with first baroclinic mode is adequate. Within this framework, we suggest a hypothesis for how radiative cooling perturbations could modify wave propagation.

Over the equatorial Indian and western Pacific Oceans, deep, precipitating convective clouds are formed due to large sea surface fluxes and/or large-scale moisture convergence. Stemming from latent heat release, Kelvin waves are excited with phase speeds slower than free Kelvin waves (see Lau and Peng 1987). As the waves propagate eastward, clouds within the wave disturbances perturb the heating profile due to radiative cooling effects. Cooling near cloud tops contributes to further destabilization of the column, thus enhancing low-level convergence within the wave disturbance. This alters the original phase speed of the wave.

Within this framework, we follow the mechanism proposed by Lau and Peng (1987), namely convective heating organized within a wave disturbance modifies the stability of the system, providing a feedback control on the phase speed of the excited wave. However, their model's internal heat source did not include a radiative component. Instead, radiative cooling was imposed uniformly across the entire wave packet via the thermodynamic energy equation, by use of a Newtonian cooling term with a 5-day radiative damping timescale. We argue that radiative cooling should be included as part of the convective heating feedback. As noted, subsequent changes in heating structure due to the radiative effects will further modify both stability and low-level convergence, thus modifying the wave's phase speed. As shown below, we consider an internal wave heat source that consists of both convective heating and radiative cooling components. Convective heating is taken to be dependent on low-level moisture convergence, while radiative cooling is parameterized in terms of a radiative damping timescale determined from a radiative–convective equilibrium model.

In the equatorial β-plane framework, linearized equations for a Kelvin wave can be written as

$$\frac{\partial u}{\partial t} + \frac{\partial \phi}{\partial x} + Du = 0, \tag{5}$$

$$\frac{\partial \phi}{\partial t} + gH\frac{\partial u}{\partial x} = Q, \tag{6}$$

where u is the perturbation zonal velocity, ϕ is the perturbation geopotential thickness, g is the gravitational acceleration, H is the equivalent depth, D is the linear momentum damping coefficient, and Q is the heating. Following Lau (1981), the above equations can be interpreted as the baroclinic component of a two-layer model where $u = u_1 - u_2$ and $\phi = \phi_1 - \phi_2$, with subscripts 1 and 2 referring to the upper and lower levels, respectively. In the context of the present study, Q represents the cumulative effect of convective heating and infrared cooling, expressed by

$$Q = \epsilon_c\frac{\partial u_2}{\partial x} - \epsilon_r\phi, \tag{7}$$

where ϵ_c is the coefficient of convective heating and ϵ_r is the radiative damping timescale. In Eq. (7), it is assumed that convective heating depends on lower level convergence (see Lau and Peng 1987). Since $(u_2 + u_1)$ is zero for a purely baroclinic mode, low-level convergence can be written as

$$\frac{\partial u_2}{\partial x} = -\frac{1}{2}\left(\frac{\partial u}{\partial x}\right). \tag{8}$$

Equation (6) can now be written as

$$\frac{\partial \phi}{\partial t} + gH\frac{\partial u}{\partial x} - \frac{\epsilon_c}{2}\left(\frac{\partial u}{\partial x}\right) + \epsilon_r\phi = 0. \tag{9}$$

Assuming the solutions take the form $u = u_o\exp[-i(wt + kx)]$ and $\phi = \phi_o\exp[-i(wt + kx)]$, where ω is angular frequency and k is wave number, Eqs. (5) and (9) can be written as

$$\omega u + k\phi + iDu = 0 \tag{10}$$

$$\omega\phi + kgHu - \frac{1}{2}\epsilon_c ku + i\epsilon_r\phi = 0. \tag{11}$$

Combining (10) and (11) yields

$$\left[\omega^2 + i(D + \epsilon_r)\omega + k^2\left(\frac{\epsilon_c}{2} - gH\right) - D\epsilon_r\right]u = 0. \tag{12}$$

For nonzero u, the solution of (12) is

$$\omega = -\frac{1}{2}(D + \epsilon_r) \pm \frac{1}{2}\left[-(D + \epsilon_r)^2 - 4\left(k^2\left(\frac{\epsilon_c}{2} - gH\right) - D\epsilon_r\right)\right]^{1/2}, \tag{13}$$

or in terms of phase speed where $C = \omega/k$,

$$C = \pm\frac{1}{2k}\left[-(D+\epsilon_r)^2 - 4\left(k^2\left(\frac{\epsilon_c}{2} - gH\right) - D\epsilon_r\right)\right]^{1/2}. \quad (14)$$

In the absence of all heating and damping, the phase speed reduces to $(gH)^{1/2}$, similar to that of free Kelvin waves associated with an equivalent depth H.

The phase speed (C_c) of waves forced only by convective heating is then

$$C_c^2 = gH - \frac{\epsilon_c}{2}. \quad (15)$$

As convective heating increases, the phase speed C_c decreases compared to the free Kelvin wave phase speed. Using (15) to rewrite (14), C can be given in terms of C_c:

$$C = C_c\left[1 - \left(\frac{D - \epsilon_r}{2kC_c}\right)^2\right]^{1/2}. \quad (16)$$

According to (16), the phase speed of forced Kelvin waves is given by C_c, modified by the dissipative term within the brackets on the rhs of (12). Our interest is to further examine how the phase speed C_c is modified by radiative cooling at the appropriate timescales. In doing so, we take D as zero, that is, no dissipation of momentum, and focus on the influence of ϵ_r based on characteristic radiative cooling rates.

To obtain an estimate of the characteristic radiative damping time ϵ_r, a one-dimensional radiative–convective equilibrium model is used. The model is similar to that of Manabe and Strickler (1964), in which they evaluated the influence of convective adjustment on a purely radiative equilibrium process. For simplicity, only the infrared cooling component is considered. Solar heating is not specified explicitly, although the surface is kept at a constant temperature of 300 K. The radiative transfer model described in section 2a is used for the calculations. Convective adjustment is invoked when a critical lapse rate of 6.5°C day^{-1} is exceeded at any level.

The atmospheric temperature and moisture profiles averaged over the equatorial Indian Ocean region for a convectively active day (15 June 1984), are used to first achieve the radiative–convective equilibrium for cloud-free conditions. The resultant solution is shown in Fig. 13. For comparison, a pure radiative–equilibrium temperature profile is also shown. Once radiative–convective equilibrium is achieved, the convective heating distribution from GATE for the convectively active phase (as shown in Fig. 12) is provided as instantaneous heating to the radiative–convective model. At the same time, cloud amount and cloud-top distribution estimates over the Indian Ocean, as obtained from the INSAT measurements for 15 June 1984, are allowed to interact with the infrared cooling process. Radiative–convective adjustment is allowed until the amplitude of the temperature perturbation introduced by the convective heating in each layer reduces to its *e*-folding value. The calculations lead to a timescale over which cloud-induced infrared cooling effects will remove temperature perturbations induced by latent heating. The idea is to identify the timescale over which radiative cooling processes can modify dynamic convergence. In the radiative–convective equilibrium model, this is accomplished simply through convective adjustment. We use this timescale for the radiative damping term ϵ_r appearing in Eq. (16). For the equatorial Indian Ocean region, we find that the radiative damping timescale is approximately 3 days, or an ϵ_r of 3.858×10^{-6} s^{-1}. This is smaller than the radiative damping timescale of 5 days that previously had been used by Chang (1977) and Lau (1981), among others.

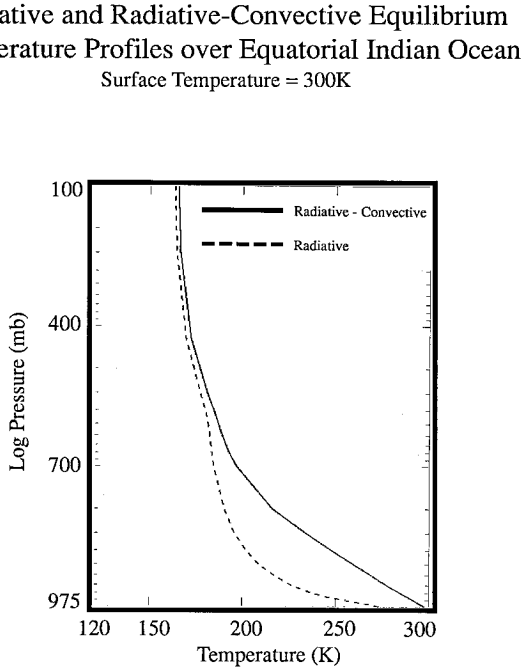

FIG. 13. Radiative–convective equilibrium solution for cloud-free conditions over equatorial Indian Ocean for surface temperature of 300 K. The pure radiative equilibrium solution is shown for comparison.

In absence of dissipation, Eq. (16) can be written as

$$C^2 = C_c^2 - \frac{\epsilon_r^2}{4k^2}. \quad (17)$$

Equation (17) indicates that the phase speed of a wave excited by convective heating will be modified by the factor $(\epsilon_r/2k)^2$. There are two possible ways in which the phase speed can be altered. When the above factor is smaller than C_c^2, radiative effects will reduce the phase speed with respect to the purely convectively forced case. For example, with a wavenumber 1 configuration, the value of $(\epsilon_r/4k)^2$ will be 151.6 m^2 s^{-2}. Thus, given a wave whose unperturbed propagation period is 30 days or an associated phase speed of C_c = 15.5 m s^{-1}, the perturbed phase speed C due to cloud-radiative effects would be 9.4 m s^{-1}, that is, a propagation period of 49

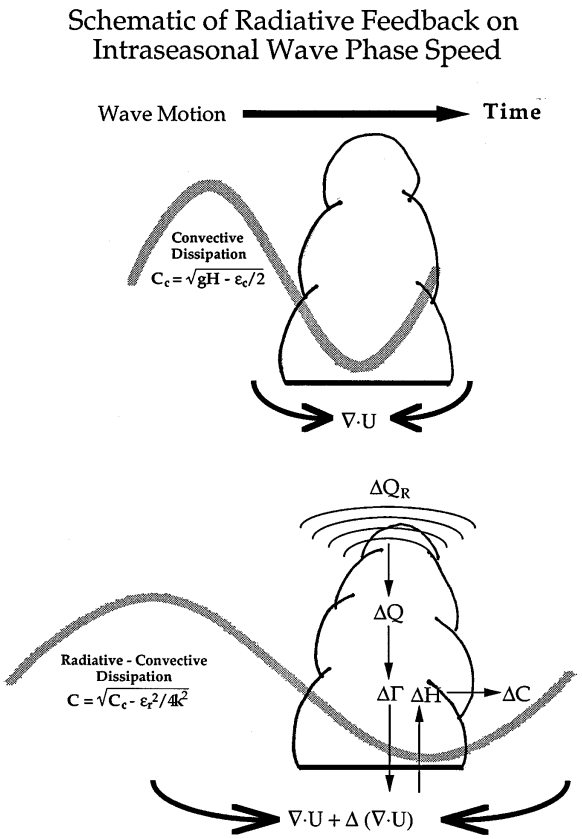

FIG. 14. Conceptual diagram of time-dependent component of Kelvin wave, with and without radiative dissipation at the same wavenumber *k*. The diagram indicates how a radiative cooling perturbation [ΔQ_R] within a convective disturbance modifies the phase speed [ΔC] of the wave excited by convective heating through sequential perturbations of the internal heating [ΔQ], stability [$\Delta\Gamma$], low-level convergence [$\Delta(\nabla \cdot \mathbf{U}$], and equivalent depth [ΔH].

days or a percentage decrease in phase speed of 60%. Alternatively, when $(\epsilon_r/4k)^2$ is greater than or larger than C_c^2, the result will be a stationary, decaying wave. Perhaps a simpler way of considering the process is to take the phase speed C of a modified wave as $(gH')^{1/2}$, where H' is the modified equivalent depth [from Eqs. (15) and (17)] and represents the result of convective–radiative feedback on dynamics that alters the phase speed of otherwise free Kelvin waves. Based on these arguments, Fig. 14 provides a simple conceptual diagram of how a radiative cooling perturbation, associated with a deep convective cloud, modifies the phase speed of an excited wave through dissipative feedback.

The above model allows for the phase speeds of Kelvin waves, such as those initiated in the Indian and western Pacific Oceans due to convective heating, to be directly modified by cloud-induced radiative cooling variations. Given the observed cloud distributions and variations in cooling rates, there is a variable range in phase speeds over which convectively triggered Kelvin waves could be propagating due to cloud-radiation feedback. That is, a broadened band of waves could appear with different speeds of propagation from the same convective source based on variations in the cooling rate structure. In doing so, it is important to note that we have not considered the role of advection on the temperature profile. The study by Weickmann and Khalsa (1990) supports our hypothesis. They find that intraseasonal waves have different phase speeds over cloudy regions of the Indian and western Pacific Oceans compared to the rest of the Tropics. Similarly, a recent modeling study of Zhao and Weare (1994) suggests that the change in intensity of convection in the course of a diurnal cycle could be a source for proliferation of phase speeds of intraseasonal waves; however, typically the diurnal variation in convection over the deep tropical oceans is relatively weak.

The question of why cloudiness varies on intraseasonal timescales remains unanswered. The intraseasonal variations of clouds themselves appear to mostly depend on the behavior of sea surface temperatures, surface fluxes, and their interaction with large-scale dynamical processes (e.g., Emanuel 1987). For a complete theory, these mechanisms need further investigation and confirmation in conjunction with more complete models of intraseasonal waves, in which all the diabatic heating components are provided in a realistic framework.

6. Summary and conclusions

In view of earlier findings that equatorial, eastward propagating, planetary-scale intraseasonal waves are a broadband phenomenon with phase speeds sensitive to the diabatic heating profile and stability of the troposphere, this study has examined the radiative cooling rate aspects of the total diabatic heating process. Radiative cooling rates are calculated over the Southeast Asian monsoon domain between 5°S–20°N and 40°–135°E at a spatial grid resolution of 5° × 5°. This is the domain where major intraseasonal waves are believed to originate. The two contrasting summer monsoon seasons of 1984 and 1987 (May–October) have been selected for investigation. Daily analyses of temperature and moisture are obtained from the European Centre for Medium Range Weather Forecasting, while cloud properties are obtained from INSAT satellite measurements and previously published work.

Detailed analyses of seasonal mean and intraseasonal variability of clouds and radiative cooling show that cooling rate profiles are directly related to the cloud distributions. During the two seasons considered here, although there is general similarity in the spatial distributions of cloudiness, there are distinct quantitative differences in cloud amounts for both total cloudiness and its decomposition into height categories. During both years, cloud amounts in the central and eastern Indian Ocean and western Pacific Ocean are between 40% and 80% with cloud tops primarily in the middle and high troposphere. Consistent with the vertical cloud distributions, seasonal mean cooling rates are as large

as 2.0°–5.0°C day^{-1} at 300–400 mb, related to the cloud-top cooling process. In the middle troposphere, between 500 and 700 mb, cooling rates range from 1.0° to 3.0°C day^{-1}. When the cooling rates are decomposed into cloud-free and cloud-induced components, the cloud-induced component tends to dominate. In this context, cloud-free cooling rates run as small as 0.5°C day^{-1}. Over the western Indian Ocean, Africa, and the Arabian Peninsula, most clouds are confined to the low and middle troposphere, with cloud amounts less than 40%. Seasonal mean cooling rates over these regions run between 2.0° and 4.0°C day^{-1} with cloud-free and cloud-induced components ranging between 1.0° and 2.0°C day^{-1}. In general, minimum cooling is found between 800 and 900 mb, largely determined by the specification of many cloud-bases at LCL heights.

Although the spatial distributions of clouds and cooling rates are very similar during the 2 years, low and middle cloud amounts over the Indian subcontinent and Indian Ocean are ~5%–10% higher during 1984 compared to 1987. Accordingly, cloud-top cooling rates in the lower troposphere are also larger by ~0.5°C day^{-1} during 1984. This is presumed to be related to Indian monsoon variability. It is well documented that rainfall over India was substantially less during 1987 as compared to 1984 (Staff Members 1985, 1988), although that observation in and of itself does not confirm the same was true over the open ocean.

During both seasons, intraseasonal variability of cloud amount is found to be largest over the equatorial Indian Ocean, the Arabian Sea, the Bay of Bengal, the South China Sea, and the western Pacific Ocean. Over these regions the percentage variance of cloud amount in a 21–76-day bandpass becomes as large as 25%–45%. The largest variances over these regions are primarily due to the variability of deep convective clouds with cloud tops above 400 mb. There are distinct episodes where the deep convective clouds go through enhanced and suppressed stages.

Intraseasonal variability of the cooling rates is found to be modulated by the variability of deep convective clouds. The centers of maximum variability are found in the middle and upper troposphere associated with cloud-top variability. Cumulative variances in 21–76-day bandpass filtered cooling rates are between 1.0° and and 2.5 (°C day^{-1})^2 or root-mean-square amplitudes between 1.0° and 1.5°C day^{-1}. Most of the variability is cloud induced. The cloud-free cooling rate component exhibits variances as low as 0.2 (°C day^{-1})^2, or a root-mean-square amplitude of 0.4°C day^{-1}.

The spatial distributions of intraseasonal variance in both cloud amount and cooling rate are similar during 1984 and 1987. However, over the equatorial Indian Ocean, the Arabian Sea, and the Bay of Bengal, intraseasonal variability is found to be much larger during 1987. Cloud amount and cooling rate amplitudes in 1987 exceed those of 1984 by 10%–15%. Notably, although the mean cloud amount and cooling rate are larger during the 1984 monsoon, intraseasonal variability is larger during 1987.

Vertical structures of the cooling rates have been examined in terms of their principal components. Over the equatorial Indian and western Pacific Oceans, the first two vertical modes of cooling contain 70%–80% of the total variance. Combination of these two modes suggest that cooling rate anomalies persist throughout the troposphere. Systematic with the cloud tops, cooling rate anomalies vary vertically within the troposphere. The first mode, which carries 50%–60% of the total variance, captures cooling rate variability due to fluctuations in deep convective clouds. This mode has a structure in which cooling rate anomalies in the upper and lower troposphere are of opposite sign, with a zero crossing between 400 and 500 mb.

The most salient point of the analysis is that the structure of the first cooling rate mode with upper and lower troposphere being out-of-phase is analogous to the zonal wind and divergent wind modes (Madden and Julian 1971; Knutson and Weickmann 1987). This suggests coupling between intraseasonal waves and radiative effects, through the conduit of deep convective clouds. Several studies have shown that latent heating within intraseasonal wave disturbances is important for maintenance and eastward propagation of the waves (see Slingo and Madden 1991 and references therein). Based on results presented here, we suggest that radiative cooling is also important. We find that variability in the radiative cooling rates perturbs the total convective heating profile in the upper and lower troposphere by 10%–30%. This has been shown by comparing radiative cooling profiles with the heating profiles obtained from GATE measurements for convectively disturbed and undisturbed cases. We suggest that once a wave is excited by convective heating, variability of clouds within the wave disturbance through radiative cooling processes further destabilizes the column, increasing low-level convergence in the wave disturbance, which through dynamic feedback modifies the wave phase speed. Since there is significant variation in the intensity of the convection and the resultant cloud-radiation interactions, both on intraseasonal and interannual timescales, the mechanism of variable radiative damping helps explain the broadband nature of intraseasonal waves.

Acknowledgments. The authors wish to thank Dr. Vikram Mehta of the NASA/Goddard Space Flight Center for helpful comments; Drs. Harry Cooper, T. N. Krishnamurti, and Noel LaSeur of The Florida State University for their helpful discussions; Dr. James Lamm and Jim Merritt for their assistance with analysis of the datasets; and Brian Swilling for assistance with preparing the figures. This research has been supported under National Science Foundation Grants ATM-88124111 and ATM-9300870. Part of the computational support has been provided by the Supercomputer Computations Research Institute at The Florida State Uni-

versity under Department of Energy Contract DOE-FCO5-85ER250000.

REFERENCES

Ackerman, S. A., and S. K. Cox, 1987: Radiative energy budget estimates for the 1979 southwest summer monsoon. *J. Atmos. Sci.,* **44,** 2052–2078.

Arkin, P. A., 1988: The global climate for June–August 1987: Mature phase of an ENSO warm episode persists. *J. Climate,* **1,** 306–324.

Bottomley, M., C. K. Folland, J. Hsiung, R. E. Newell, and D. A. Parker, 1990: *Global Ocean Surface Temperature Atlas.* Her Majesty's Stationery Office, 333 pp.

Chang, C. P., 1977: Viscous internal gravity waves and low-frequency oscillations in the Tropics. *J. Atmos. Sci.,* **34,** 901–910.

——, and H. Lim, 1988: Kelvin wave-CISK: A possible mechanism for the 30–50 day oscillations. *J. Atmos. Sci.,* **45,** 1709–1720.

Clough, S. A., F. X. Kneizys, L. S. Rothman, and W. O. Gallery, 1981: FASCO01b. *Soc. Photo-Opt. Instrum. Eng.,* **277,** 152–166.

Cogan, J. L., and J. H. Willand, 1976: Measurements of sea surface temperature by the NOAA 2 satellite. *J. Appl. Meteor.,* **15,** 173–180.

Cox, S. K., and K. T. Griffith, 1979a: Estimates of radiative divergence during Phase III of the GARP Atlantic Tropical Experiment: Part I. Methodology. *J. Atmos. Sci.,* **36,** 576–585.

——, and ——, 1979b: Estimates of radiative divergence during Phase III of the GARP Atlantic Tropical Experiment: Part II. Analysis of Phase III Results. *J. Atmos. Sci.,* **36,** 586–601.

Desbois, M. D., G. Seze, and G. Szejwach, 1982: Automatic classification of clouds on METEOSAT imagery: Application to high-level clouds. *J. Appl. Meteor.,* **21,** 401–412.

Dopplick, T. G., 1972: Radiative heating of the global atmosphere. *J. Atmos. Sci.,* **29,** 1278–1294.

Ellingson, R. G., J. Ellis, and S. Fells, 1991: The intercomparison of radiation codes used in climate models: Longwave results. *J. Geophys. Res.,* **96,** 8929–8953.

Emanuel, K. A., 1987: An air–sea interaction model of intraseasonal oscillations in the Tropics. *J. Atmos. Sci.,* **44,** 2324–2340.

Frank, W. M., and J. L. McBride, 1989: The vertical distribution of heating in AMEX and GATE cloud clusters. *J. Atmos. Sci.,* **46,** 3464–3478.

Frouin, R., C. Gautier, and J. J. Morcrette, 1988: Downward longwave irradiance at the ocean surface from satellite data: Methodology and in situ validation. *J. Geophys. Res.,* **93,** 597–619.

Goody, R., 1952: A statistical model for water vapor absorption. *Quart. J. Roy. Meteor. Soc.,* **62,** 31–35.

Goswami, B. N., and J. Shukla, 1984: Quasi-periodic oscillations in a symmetric general circulation model. *J. Atmos. Sci.,* **41,** 3058–3067.

Hayashi, Y., and A. Sumi, 1986: The 30–50 day oscillations simulated in ''aqua planet'' model. *J. Meteor. Soc. Japan,* **64,** 451–467.

Hendon, H. H., 1988: A simple model of the 40–50 day oscillation. *J. Atmos. Sci.,* **45,** 569–584.

——, and M. L. Salby, 1994: The life cycle of the Madden–Julian oscillation. *J. Atmos. Sci.,* **51,** 2225–2237.

Houze, R. A., 1993: *Cloud Dynamics.* Academic Press, 573 pp.

Johnson, R. H., and R. A. Houze, 1987: Precipitating cloud systems of the Asian monsoon. *Monsoon Meteorology, Oxford Monogr. on Geology and Geophysics,* No. 7, Oxford Press, 293–353.

Katayama, A., 1967: On the radiation budget of the troposphere over the Northern Hemisphere (III). *J. Meteor. Soc. Japan,* **45,** 26–39.

Kiladis, G. N., and K. M. Weickmann, 1992: Circulation anomalies associated with tropical convection during northern winter. *Mon. Wea. Rev.,* **120,** 1900–1923.

Knutson, T. R., and K. M. Weickmann, 1987: 30–60 day atmospheric oscillations: Composite life cycles of convection and circulation anomalies. *Mon. Wea. Rev.,* **115,** 1407–1436.

Krishnamurti, T. N., D. Oosterhof, and A. Mehta, 1988: Air–sea interaction on the timescale of 30 to 50 days. *J. Atmos. Sci.,* **45,** 1304–1319.

Lamm, J. E., A. V. Mehta, E. A. Smith, and R. Jenne, 1991: Description of the U.S. INSAT satellite data set (April 1984 to March 1989). Tech. Publ., 60 pp. [Available from Dept. of Meteorology and Supercomputer Computations Research Institute, The Florida State University, Tallahassee, FL 32306.]

Lau, K. M., 1981: Oscillations in a simple equatorial climate system. *J. Atmos. Sci.,* **38,** 248–261.

——, and P. H. Chan, 1986: Aspects of the 40–50 day oscillation during the northern summer as inferred from outgoing longwave radiation. *Mon. Wea. Rev.,* **114,** 1354–1367.

——, and L. Peng, 1987: Origin of low frequency (intraseasonal) oscillations in the tropical atmosphere. Part I: The basic theory. *J. Atmos. Sci.,* **44,** 950–972.

——, P. J. Sheu, and I. S. Kang, 1994: Multiscale low-frequency circulation modes in the global atmosphere. *J. Atmos. Sci.,* **51,** 1169–1193.

Lau, N. C., I. M. Held, and J. D. Neelin, 1988: The Madden–Julian oscillations in an idealized general circulation model. *J. Atmos. Sci.,* **45,** 3810–3831.

Legler, D. M., 1983: Empirical orthogonal function analysis of wind vectors over the tropical Pacific region. *Bull. Amer. Meteor. Soc.,* **64,** 234–241.

——, 1984: Response to ''Comments on empirical orthogonal function analysis of wind vectors over the tropical Pacific region.'' *Bull. Amer. Meteor. Soc.,* **65,** 162.

Luther, F. N., R. G. Ellingson, Y. Fouquart, S. Fells, N. Scott, and W. J. Wiscombe, 1988: Intercomparison of radiation codes in climate models (ICRCCM): Longwave clear-sky results—A workshop summary. *Bull. Amer. Meteor. Soc.,* **69,** 40–48.

Madden, R. A., and P. R. Julian, 1971: Detection of a 40–50 day oscillation in the zonal wind in the tropical Pacific. *J. Atmos. Sci.,* **28,** 702–708.

——, and ——, 1994: Observations of the 40–50-day tropical oscillation—A review. *Mon. Wea. Rev.,* **122,** 814–837.

Malkmus, W., 1967: Random Lorentz band model with exponential tailed S-1 line intensity distribution function. *J. Opt. Soc. Amer.,* **57,** 323–329.

Manabe, S., and R. F. Strickler, 1964: Thermal equilibrium of the atmosphere with a convective adjustment. *J. Atmos. Sci.,* **21,** 361–384.

McClatchey, R. A., R. W. Fenn, J. E. A. Selby, F. E. Volz, and J. S. Garing, 1972: Optical properties of the atmosphere. 3d ed. AFCRL Environmental Research Papers 411, 108 pp.

Mehta, A. V., 1991: Intraseasonal variability of infrared cooling rates during the Asian summer monsoon and their influence on intraseasonal waves. Ph.D. dissertation, The Florida State University, 166 pp. [Available from Dept. of Meteorology, The Florida State University, Tallahassee, FL 32306.]

——, and T. N. Krishnamurti, 1988: Interannual variability of the 30 to 50 day wave motions. *J. Meteor. Soc. Japan,* **66,** 535–547.

Mehta, V. M., and J. E. Ahlquist, 1986: Interannual variability of the 30–50 day activity in the Indian summer monsoon. *Meteor. Atmos. Phys.,* **35,** 166–176.

Morcrette, J. J., 1990: Impact of changes to the radiative transfer parameterizations plus cloud optical properties in the ECMWF model. *Mon. Wea. Rev.,* **118,** 847–873.

Murakami, T., L. X. Chen, A. Xie, and M. L. Shrestha, 1986: Eastward propagation of 30–60-day perturbations as revealed from outgoing longwave radiation data. *J. Atmos. Sci.,* **43,** 961–971.

Paltridge, G. W., and C. M. R. Platt, 1981: Aircraft measurements of solar and infrared radiation and the microphysics of cirrus clouds. *Quart. J. Roy. Meteor. Soc.,* **107,** 367–380.

Prupracher, H. R., and J. D. Klett, 1980: *Microphysics of Clouds and Precipitation.* D. Reidel, 714 pp.

Ramanathan, V., 1987: The role of earth radiation budget studies in climate and general circulation research. *J. Geophys. Res.,* **92,** 4075–4095.

Reed, R. J., and E. E. Recker, 1971: Structure and properties of synoptic-scale wave disturbances in the equatorial western Pacific. *J. Atmos. Sci.,* **28,** 1117–1123.

Rossow, W. B., 1989: Measuring cloud properties from space: A review. *J. Climate,* **2,** 201–213.

——, and Coauthors, 1985: ISCCP cloud analysis algorithm intercomparison. *J. Climate Appl. Meteor.,* **24,** 877–903.

——, A. W. Walker, and L. C. Garder, 1993: Comparison of ISCCP and other cloud amounts. *J. Climate,* **6,** 2394–2418.

Rui, H., and B. Wang, 1990: Development characteristics and dynamic structure of tropical intraseasonal convection anomalies. *J. Atmos. Sci.,* **47,** 357–379.

Sellers, W. D., 1965: *Physical Climatology*. University of Chicago Press, 272 pp.

Sikka, D. R., and S. Gadgil, 1980: On the maximum cloud zone and the ITCZ over Indian longitudes during the southwest monsoon. *Mon. Wea. Rev.,* **108,** 1840–1853.

Slingo, A., and J. Slingo, 1988: The response of a general circulation model to cloud longwave radiative forcing. I: Introduction and initial experiments. *Quart. J. Roy. Meteor. Soc.,* **114,** 1027–1062.

Slingo, J. M., and R. A. Madden, 1991: Characteristics of the tropical intraseasonal oscillation in the NCAR community climate model. *Quart. J. Roy. Meteor. Soc.,* **117,** 1129–1169.

Smith, E. A., 1984: Radiative forcing of the southwest summer monsoon: A satellite perspective. Ph.D. dissertation, Colorado State University, 520 pp. [Available from Dept. of Atmospheric Sciences, Colorado State University, Fort Collins, CO 80523.]

——, and D. R. Sikka, 1987: The coherence of satellite infrared temperatures with monsoon rainfall at preferred frequencies and the triplex behavior of the Indian summer monsoon. *Meteor. Atmos. Phys.,* **37,** 219–236.

——, and M. R. Smith, 1987: Interannual variability of the tropical radiation balance and the role of extended cloud systems. *J. Atmos. Sci.,* **44,** 3210–3234.

——, and A. V. Mehta, 1990: The role of organized tropical storms and cyclones on intraseasonal oscillations in the Asian monsoon domain based on INSAT satellite measurements. *Meteor. Atmos. Phys.,* **44,** 195–218.

——, and L. Shi, 1992: Surface forcing of the infrared cooling profile over the Tibetan Plateau. Part I: Influence of relative longwave radiation heating at high altitude. *J. Atmos. Sci.,* **49,** 805–822.

——, and ——, 1995: Reducing discrepancies in atmospheric heat budget of the Tibetan Plateau by satellite-based estimates of radiative cooling and cloud-radiation feedback. *Meteor. Atmos. Phys.,* **56,** 229–260.

——, M. R. Smith, and K. W. Oh, 1989: A PC-based interactive imaging system designed for INSAT data analysis and monsoon studies. *Bull. Amer. Meteor. Soc.,* **70,** 1105–1122.

Staff Members, 1985: Weather—Monsoon season (June–September, 1984). *Mausam,* **36,** 393–402.

——, 1988: Weather—Monsoon season (June–September, 1987). *Mausam,* **39,** 393–402.

Stephens, G. L., 1978a: Radiation profiles in extended water clouds. I: Theory. *J. Atmos. Sci.,* **35,** 2111–2122.

——, 1978b: Radiation profiles in extended water clouds. II: Parameterization schemes. *J. Atmos. Sci.,* **35,** 2123–2132.

——, S. C. Tsay, P. W. Stackhouse, and P. J. Flatau, 1990: The relevance of the microphysical and radiative properties of cirrus clouds to climate and climatic feedback. *J. Atmos. Sci.,* **47,** 1742–1753.

Stowe, L. L., C. A. Welleneger, T. F. Eck, H. Y. M. Yeh, and the *Nimbus-7* Cloud Data Processing Team, 1988: *Nimbus-7* global cloud climatology. Part I: Algorithms and validation. *J. Climate,* **1,** 445–470.

Sui, C. H., and K. M. Lau, 1989: Origin of low-frequency (intraseasonal) oscillations in the tropical atmosphere. Part II: Structure and propagation of mobile wave-CISK modes and their modification by lower boundary forcing. *J. Atmos. Sci.,* **46,** 37–56.

Swinbank, R., T. N. Palmer, and M. K. Davey, 1988: Numerical simulations of the Madden and Julian oscillation. *J. Atmos. Sci.,* **45,** 774–788.

Thompson, R. M., Jr., S. W. Payne, E. E. Recker, and R. J. Reed, 1979: Structure and properties of synoptic-scale wave disturbances in the intertropical convergence zone of the eastern Atlantic. *J. Atmos. Sci.,* **36,** 53–72.

Warren, S. A., C. J. Hahn, and J. London, 1985: Simultaneous occurrence of different cloud types. *J. Climate Appl. Meteor.,* **24,** 658–667.

Weickmann, K. M., and S. J. S. Khalsa, 1990: The shift of convection from the Indian Ocean to the western Pacific Ocean during a 30–60 day oscillation. *Mon. Wea. Rev.,* **118,** 964–978.

——, G. R. Lussky, and J. E. Kutzbach, 1985: Intraseasonal (30–60 day) fluctuations of outgoing longwave radiation and 250 mb streamfunction during northern winter. *Mon. Wea. Rev.,* **113,** 941–961.

Yanai, M., S. Esbensen, and J. Chu, 1973: Determination of bulk properties of tropical cloud clusters from large-scale heat and moisture budgets. *J. Atmos. Sci.,* **30,** 611–627.

Yasunari, T., 1980: A quasi-stationary appearance of 30 to 40 day period in the cloudiness fluctuations during the summer monsoon over India. *J. Meteor. Soc. Japan,* **58,** 225–227.

Zhao, Y., and B. C. Weare, 1994: The effect of diurnal variation of cumulus convection on large-scale low-frequency oscillations in the Tropics. *J. Atmos. Sci.,* **51,** 2653–2663.

Zhu, B., and B. Wang, 1993: The 30–60-day convection seesaw between the tropical Indian and western Pacific Oceans. *J. Atmos. Sci.,* **50,** 184–199.